$BaTiO_3$ BASED FERROELECTRIC MATERIALS FOR ELECTROCALORIC COOLING APPLICATIONS

A Thesis Submitted to
The Graduate School of Engineering and Science of
İzmir Institute of Technology
in Partial Fulfillment of the Requirements for the Degree of

MASTER OF SCIENCE

in Materials Science and Engineering

by
Keriman ŞANLI

December 2018
İZMİR

We approve the thesis of **Keriman ŞANLI**

Examining Committee Members:

Asst. Prof. Dr. Umut ADEM
Department of Materials Science and Engineering, İzmir Institute of Technology

Prof. Dr. Muhsin ÇİFTÇİOĞLU
Department of Chemical Engineering, İzmir Institute of Technology

Assoc. Prof. Dr. Emre YALAMAÇ
Department of Metallurgical and Materials Engineering, Celal Bayar University

27 December 2018

Asst. Prof. Dr. Umut ADEM
Supervisor, Department of Materials Science and Engineering, İzmir Institute of Technology

Assoc. Prof. Dr. Yaşar AKDOĞAN
Co-Supervisor, Department of Materials Science and Engineering, İzmir Institute of Technology

Prof. Dr. Mustafa Muammer DEMİR
Head of the Department of Materials Science and Engineering

Prof. Dr. Aysun SOFUOĞLU
Dean of the Graduate School of Engineering and Sciences

ACKNOWLEDGEMENTS

It is a great pleasure to thank all those who encouraged and supported me during this study. First of all, I would like to thank to my advisor Dr. Umut Adem for his valuable knowledge and support in every part of this study. I could not have succeeded without his belief in me.

I would like to thank Turkish Scientific and Technological Research Council (TÜBİTAK) via the project with the number 315M241 and IZTECH for supporting me during this project.

Furthermore, I am very thankful to Mrs. Işın Özçelik who made XRD experiments with great precision. She is open to all kinds of ideas and different measurement methods. Also, I would like to thank to the experts working in the Material Research Center in IZTECH for SEM images.

I am very honored to thank to my mother Mrs. Filiz Erkanlı and my sister Mrs. Canan Kurt who are happy with my accomplishments throughout my life and think my future more than me. The most meaningful thing in the world is always to feel their belief in me. I would also like to thank my nephews who always motivated me with their love.

I would be honored to thank to Ms. Tuğçe Demirtay for whom I have been working since the beginning of this work. Her presence gave me strength in all circumstances and at any time.

Last but not least, I would like to thank my dear friend Mr. Berk Yıldırım who has beautified my life with his presence.

ABSTRACT

$BaTiO_3$ BASED FERROELECTRIC MATERIALS FOR ELECTROCALORIC COOLING APPLICATIONS

The aim of this project was to produce electrocaloric materials and to determine the potential of these materials for electrocaloric cooling applications.

The electrocaloric effect (ECE) of lead-free $Ba_{0.8}Sr_{0.2}Ti_{1-x}Zr_xO_3$ ($0 \leq x \leq 0.10$) ferroelectric ceramics was studied. The phase analysis of each ceramic composition that was synthesized by conventional solid-state reaction technique was performed by X-ray Diffraction. Dielectric measurements were done to determine the phase transition temperatures (Curie temperature, T_c) of all compositions and also construct a phase diagram. ΔT values were calculated indirectly using electrical polarization curves measured at different temperatures and Maxwell's equations.

ΔT values that were obtained from different regions of the phase diagram are compared. The most suitable composition for applications was chosen considering the ΔT value, temperature range where relatively large ΔT is preserved and the Curie temperature of all ceramics. $Ba_{0.8}Sr_{0.2}Ti_{0.93}Zr_{0.07}O_3$ ceramic located near the critical point shows the best performance with ΔT value of 0.40 K under 20 kV/cm. In comparison with the lead-free ceramics studied in the literature, $Ba_{0.8}Sr_{0.2}Ti_{1-x}Zr_xO_3$ system can be considered as one of the best candidates for future electrocaloric cooling technologies.

ÖZET

ELEKTROKALORİK SOĞUTMA UYGULAMALARI İÇİN $BaTiO_3$ TEMELLİ FERROELEKTRİK MALZEMELER

Bu projenin amacı elektrokalorik soğutma uygulamaları için elektrokalorik malzemeler üretmektir.

Bu tezde kurşun içermeyen $Ba_{0.8}Sr_{0.2}Ti_{1-x}Zr_xO_3$ $(0 \leq x \leq 0.10)$ ferroelektrik seramiklerinin elektrokalorik etkisi araştırılmıştır. Herbir seramik kompozisyonu geleneksel katı hal reaksiyon yöntemiyle sentezlenmiş olup, seramiklerin faz analizi X-ışını Kırınımı metoduyla yapılmıştır. Dielektrik ölçümler kullanılarak kompozisyonların faz geçiş sıcaklıkları (Curie sıcaklığı, T_c) belirlenmiş ve böylece elde edilen değerler kullanılarak faz diyagramı oluşturulmuştur. Tüm seramik örnekleri için, sıcaklığa bağlı elektriksel kutuplanma eğrileri ve Maxwell denklemleri kullanılarak elektrokalorik sıcaklık değişimi (ΔT) dolaylı olarak hesaplanmıştır.

Sonuç olarak faz diyagramının farklı bölgelerinden elde edilen ΔT değerleri karşılaştırılmıştır. T_c değerinin oda sıcaklığına yakınlığı, elektrokalorik etkinin yüksek olduğu sıcaklık aralığının genişliği ve ΔT değerinin büyüklüğü değerlendirilerek en uygun kompozisyon seçilmiştir. Kritik noktanın yakınında bulunan $Ba_{0.8}Sr_{0.2}Ti_{0.93}Zr_{0.07}O_3$ malzemesinin, 20 kV/cm elektrik alan altında elde edilen ve geniş bir sıcaklık aralığına yayılan EC sıcaklık değişiminin (0.40 K) en iyi performansı gösterdiği düşünülmektedir. Elde edilen ΔT değerleri literatürdeki değerlerle karşılaştırıldığında $Ba_{0.8}Sr_{0.2}Ti_{1-x}Zr_xO_3$ $(0 \leq x \leq 0.10)$ sisteminin elektrokalorik soğutma teknolojileri için gelecek vadeden bir sistem olduğunu söylemek mümkündür.

TABLE OF CONTENTS

LIST OF FIGURES viii

LIST OF TABLES x

CHAPTER 1. INTRODUCTION 1
1.1. Electrocaloric Effect 1
1.1.1. History 1
1.1.2. Phenomenological & Thermodynamical Description 2
1.1.3. Applications 4
1.2. Electrocaloric Materials 6
1.3. Properties of Electrocaloric Materials 7
1.3.1. Ferroelectric Properties 10
1.4. Measurement Methods 15
1.4.1. Direct Measurement 15
1.4.2. Indirect Measurement 15
1.5. Physical Mechanisms for ECE 16
1.5.1. First Order vs. Diffuse Phase Transition 17
1.5.2. Critical Point 17
1.5.3. Relaxors 18
1.6. Motivation of Thesis 19

CHAPTER 2. EXPERIMENTAL METHODS 21
2.1. Material Preparation 21
2.2. Characterization of the Materials 21
2.2.1. Particle Size Analysis 23
2.2.2. Phase Analysis 23
2.2.3. Microstructural Analysis 23
2.2.4. Density Measurements 24
2.3. Electrical Measurements 25

2.3.1. Dielectric Constant Measurements 25
2.3.2. Polarization Measurements 26

CHAPTER 3. RESULTS AND DISCUSSION 27
3.1. Phase Analysis 27
3.2. Particle Size Analysis 29
3.3. Microstructural Analysis 30
3.4. Dielectric Measurements 32
3.5. Polarization Measurements 37
3.6. Calculation of the Electrocaloric Temperature Change 38

CHAPTER 4. CONCLUSIONS 47

REFERENCES 48

LIST OF FIGURES

Figure **Page**

Figure 1.1. Schematic representation of electrocaloric cooling cycle in a dielectric material. 2

Figure 1.2. Schematic presentation of the EC solid-state cooling cycle (left) and traditional vapor-compression cooling cycle (right).....3

Figure 1.3. Distribution of the gases in atmosphere. 4

Figure 1.4. The history of atmospheric concentrations of CFCs during 1940-2005. 5

Figure 1.5. (a) A flexible EC device and (b) temperature change of overheated smartphone battery with and without an EC device. 6

Figure 1.6. The suitable A and B site substitutions for $BaTiO_3$ and their effect on transition temperatures.....9

Figure 1.7. Venn diagram showing the relation between dielectrics, piezoelectrics, pyroelectrics and ferroelectrics 10

Figure 1.8. Ideal hysteresis loop of a ferroelectric material. 11

Figure 1.9. Comparison of (a) hyteresis curves (b) phase transition behaviour and (c) dielectric behaviour of the normal ferroelectrics and relaxor ferroelectrics. 14

Figure 1.10. Schematic temperature dependence of the dielectric permittivity and spontaneous polarization P_s for a ferroelectric with (a) a first-order and (b) a second-order and (c) for a relaxor ferroelectric. 17

Figure 1.11. (a) Temperature dependence of dielectric constant at 100 Hz and (b) the phase diagram of BHT ceramics.....18

Figure 1.12. (a) Dielectric constant values for $BSTZ_x$ ceramics ($0 \leq x \leq 0.10$) and dielectric loss for x=0.01 as a function of temperature at 1 kHz. Inset shows diffuseness exponent, γ and Zr content. (b) Temperature-Composition (T-x) phase diagram of $BSTZ_x$ ceramics for $0 \leq x \leq 0.10$. 20

Figure 2.1. Flow chart of the synthesis. 22

Figure 2.2. Sample holder used in electrical measurements. 25

Figure 3.1. XRD patterns of calcined $BSTZ_x$ samples for $0 \leq x \leq 0.10$ in the range of 2Θ (a) from 20° to 80° and (b) close examination between 43°-48°.....27

Figure 3.2. XRD patterns of sintered $BSTZ_x$ samples for $0 \leq x \leq 0.10$ in the range of 2Θ (a) from 20° to 80° and (b) close examination between 43°-48°.....28

Figure 3.3. Particle size distribution for $BSTZ_x$ samples after calcination.....29

Figure 3.4. SEM micrographs of $BSTZ_x$ ceramics for (a) x=0, (b) x=0.03, (c) x=0.05, (d) x=0.07, and (e) x=0.10.....31

Figure 3.5. Temperature dependence of dielectric constant of $BSTZ_x$ ceramics for (a) x=0, (b) x=0.03, (c) x=0.05, (d) x=0.07, and (e) x=0.10.....33

Figure 3.6. Temperature dependence of dielectric constant (a) and dielectric loss (b) at 1 kHz for the $BSTZ_x$ ceramics with x=0, x=0.03, x=0.05, x=0.07, and x=0.10. 34

Figure 3.7. The inverse dielectric constant plotted at 1 kHz as a function of temperature (a) and the double logarithmic plot to deduce diffuseness constant, γ (b) for undoped BST ceramic (the square symbols denote the experimental data and the solid line denotes the linear fits using the Curie-Weiss law). 35

Figure 3.8. Diffuseness constants (γ) of $BSTZ_x$ ceramics.....35

Figure 3.9. Phase diagram of $BSTZ_x$ ceramics for $0 \leq x \leq 0.10$; black symbols are data points of the phase transition temperatures from the reference study and red symbols are data points of the phase transition temperatures determined using dielectric measurements in this study. 36

Figure 3.10. The P-E loops of $BSTZ_x$ ceramics for (a) x=0, (b) x=0.03, (c) x=0.05, (d) x=0.07, (e) x=0.10 and (f) comparison of all ceramics at 24°C and 1 Hz. 38

Figure 3.11. The P-T curves of $BSTZ_x$ with (a) x=0, (b) x=0.03, (c) x=0.05, (d) x=0.07, (e) x=0.10 at various electric fields and 1 Hz and (f) comparison of remanent polarization of all compositions.....39

Figure 3.12. Numerically calculated ΔT-T curves of $BSTZ_x$ with (a) x=0, (b) x=0.03, (c) x=0.05, (d) x=0.07, (e) x=0.10 at various electric fields and 1 Hz and (f) comparison of ΔT-T for all ceramics at 20 kV/cm. 41

Figure 3.13. Temperature dependence of (a) ΔT and (b) ΔS at 20 kV/cm and 1 Hz. 42

Figure 3.14. Fitted P-T curves of $BSTZ_x$ with (a) x=0, (b) x=0.03, (c) x=0.05, (d) x=0.07, (e) x=0.10 at 20 kV/cm electric field and 1 Hz. 43

Figure 3.15. Fitted ΔT-T curves of $BSTZ_x$ with (a) x=0, (b) x=0.03, (c) x=0.05, (d) x=0.07, (e) x=0.10 at various electric fields and 1 Hz and (f) comparison of the fitted ΔT-T for all ceramics at 20 kV/cm.....44

LIST OF TABLES

Table **Page**

Table 1.1. The electrocaloric responses of the most important lead-containing and lead-free materials. 8

Table 3.1. Density values of sintered $BSTZ_x$ samples for $0 \leq x \leq 0.10$ 30

Table 3.2. X-ray energies of Ba, Ti, Zr and Sr elements. 32

Table 3.3. Hysteresis loop parameters of the $BSTZ_x$ ceramics 37

Table 3.4. Comparison of the ECE properties of the $BSTZ_x$ ceramics studied in this work with those in the literature. 45

CHAPTER 1

INTRODUCTION

1.1. Electrocaloric Effect

Due to growing industry demand and increasing living standards, the cooling market has become a constantly growing large market. In the recent years, the significant increase in the use of refrigeration has led to the consumption of non-renewable energy sources and climate change. In order to reduce environmental problems such as global warming and the amount of halocarbon gases in the atmosphere, the efficiency of the cooling technologies of cryogenic refrigerators, air conditioners and refrigerators should be increased considerably.

In addition to the need for increased energy efficiency, other environmental issues such as operating noise, use of environmentally harmful refrigerant chemicals make the need for more efficient alternative cooling technologies inevitable. Therefore, studies on the development of alternative technologies such as magnetocaloric and electrocaloric cooling have been given importance. Although magnetocaloric cooling has been studied for a long time, the studies on electrocaloric cooling have only recently been growing. The most important advantage of electrocaloric cooling compared to magnetocaloric cooling is that the electric field (voltage) required for electrocaloric cooling is easier to apply (consumes less energy) compared to the high magnetic fields required for magnetic cooling.[1]

1.1.1. History

The electrocaloric effect (ECE) was firstly observed by Kobeko and Kurtschatov on crystals of Rochelle Salt in 1930. The effect was also discovered on potassium dihydrogen phosphate (KDP) in 1950, at that time it was not an option for electrocaloric cooling applications because of the small ΔT values. First research to use this effect started in 1956 and continued in the 1960s and 1970s but due to the absence of

significant electrocaloric temperature change (lower 1K), research interest in electrocaloric materials declined.

The ECE gained interest again in the 2000s after Mischenko et al. observed large ECE (ΔT=12 K) on PZT thin films which was called giant ECE.[2] This was followed by more studies on oxide and polymer thin films. Estimation of the ECE is typically done by an indirect method which utilizes measurements of electrical polarization as a function of electric field at different temperatures as will be described later. Besides the progress of indirect measurements techniques in 2000s[3–5], few direct measurement systems started to emerge.[6–8]

1.1.2. Phenomenological & Thermodynamical Description

The principle of the Electrocaloric Effect (ECE) is related to changes in temperature and isothermal entropy induced by the change in polarization of a dielectric material with an external electric field, under adiabatic conditions.[9]

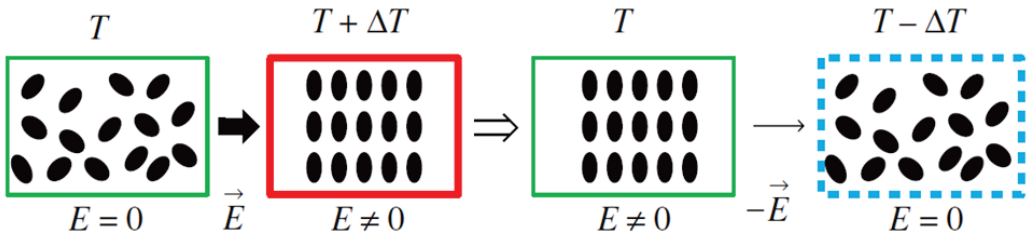

Figure 1.1. Schematic representation of electrocaloric cooling cycle in a dielectric material.[10]

The application (or removal) of the electric field orients the dipoles of the polar material and accordingly causes an increase (or decrease) in the net polarization. This causes a decrease in entropy of the dipolar subsystem, leading to an increase in temperature to prevent total entropy change. If the electric field is removed from the system, the entropy increases and as a result the temperature falls to the initial temperature. Therefore ECE is reversible. Schematic representation as described in Figure 1.1 summarizes the basic principle of the ECE.

Figure 1.2 shows the stages of the EC cooling cycle and the traditional vapor-compression cooling system and also the differences between them. Vapor-compression technology has been used predominantly in cooling devices since the 19th century. The

general operating principle of this system is summarized as the conversion of the refrigerant gas into the liquid form under pressure and the release of latent heat due to the phase transition. When the pressure is removed, the refrigerant converts back into the gas form and the latent heat is reabsorbed and the environment cools down.[11] The EC cooling follows vapor-compression systems and includes the same stages as the reverse Carnot cycle.

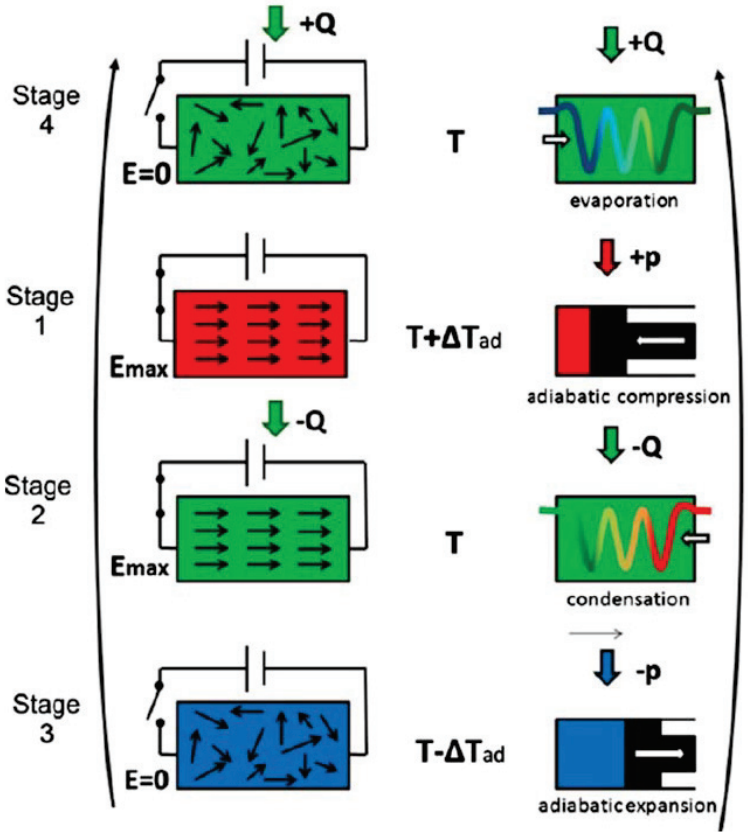

Figure 1.2. Schematic presentation of the EC solid-state cooling cycle (left) and traditional vapor-compression cooling cycle (right).[1]

In the first stage known as the adiabatic polarization, dipoles in an EC material are aligned by the electric field and EC material heats up to prevent total entropy change. This stage is similar to the adiabatic compression of a refrigerant in the compressor of traditional vapor compression refrigerator.

The second stage is called isoelectric enthalpic transfer. The electric field is continued to be applied in order to prevent the dipoles from reabsorbing the heat while the heat is removed from the system. This stage corresponds to the isothermal

compression of the refrigerant in the compressor unit of the vapor compression refrigerator.

In the third stage called adiabatic depolarization, the removal of the electric field causes the dipoles to become unoriented. There is a flow of energy from the thermal entropy to the dipole entropy and the temperature of the EC material decreases. This stage corresponds to the expansion of the refrigerant in an adiabatic expander of vapor compression refrigerator.

The last stage known as isoelectric entropic transfer closes the Carnot cycle. The electric field is not applied as in the third stage. Since the EC material is cooler than the environment, the heat is transferred from the cold reservoir to the working EC material. This is equivalent to the isothermal expansion of the refrigerant in the evaporator of vapor compression refrigerator.[1]

1.1.3. Applications

As mentioned above, traditional vapor-compression refrigeration systems require a refrigerant gas with high global-warming potential (GWP) such as hydrofluorocarbons and hydrochlorofluorocarbons.[11] The pie chart in Figure 1.3 shows the distribution of gases in the atmosphere. It can be observed that the amount of halocarbons that triggers global warming is considerable.

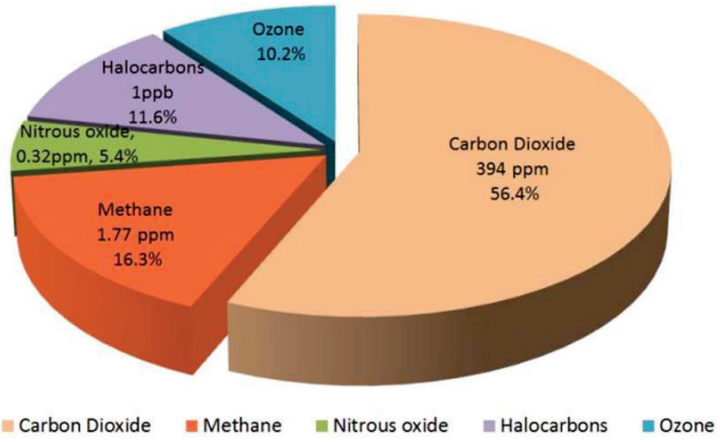

Figure 1.3. Distribution of the gases in atmosphere.[12]

When Figure 1.4 which shows the increase of these gases over the years is examined, it can easily be said that the increase in the use of traditional cooling

technologies causes this. It is particularly alarming that consumers in developing countries continue to use low-performance vapor-compression cooling technologies and pose a threat to the atmosphere.

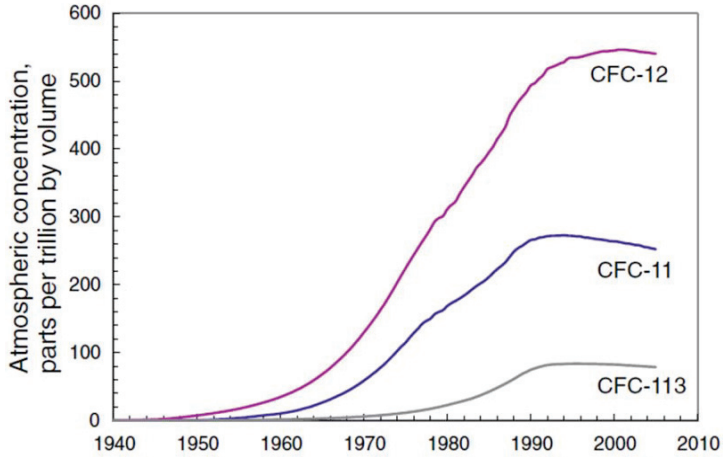

Figure 1.4. The history of atmospheric concentrations of CFCs during 1940-2005.[13]

Because of the negative effects of existing cooling technologies on the environment, studies on more environmentally friendly alternatives have accelerated. For this purpose, several consortiums have been established to support alternative cooling technologies. The most important of these consortiums is CaloriCoolTM, a caloric material consortium based on private sector and university cooperation. The purpose of this consortium, which includes key research groups such as Pacific Northwest and Oak Ridge National Laboratories, University of Maryland, Pennsylvania State University, GE Global Research, United States Research Center, Astronautics Corporation of America, and Citrine Informatics, is to develop a device for testing caloric materials.

In addition to the works carried out in the consortium, many research groups focused on prototype studies. The EC device shown in Figure 1.5, produced by a group at the University of California, is among the most important of these studies. Figure 1.5 (a) shows the thin and flexible EC device produced using P (VDF-TrFE-CFE) polymer. This device can be used to prevent heating of smartphones and laptops.[14]

Li batteries used in smartphones under high workload create a fire hazard. Also, thermal overload reduces battery life and causes fatigue in other components of the smartphone. Figure 1.5 (b) shows the difference in the temperature of the Li battery with and without EC device. Under high workload, Li batteries heat up to 52.5°C. When

allowed to cool in the air, the temperature decreases by 3°C in 50 s without the use of EC device, but with the EC device, the temperature decreases by 8°C in the first 5 s. Thus, it is seen that the EC device helps to solve the problem caused by the overheating of Li batteries.[14]

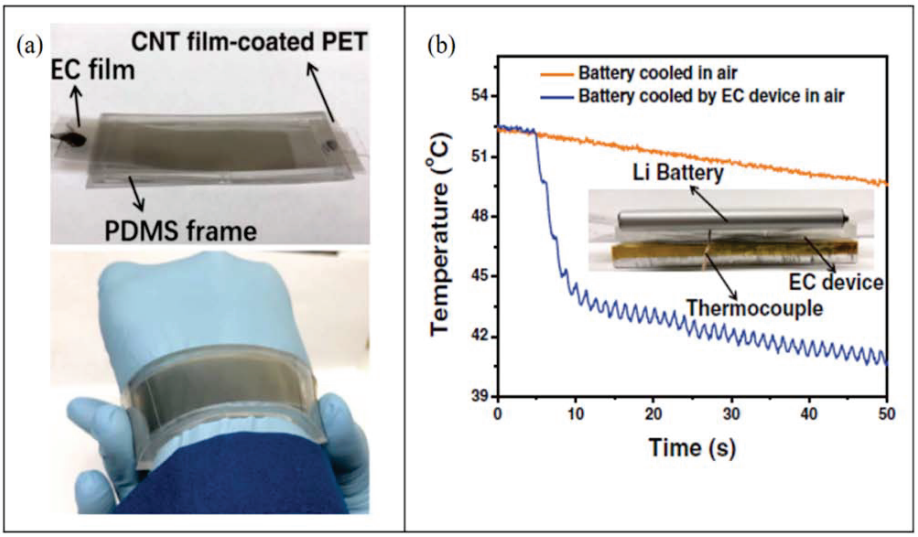

Figure 1.5. (a) A flexible EC device and (b) temperature change of overheated smartphone battery with and without an EC device.[14]

1.2. Electrocaloric Materials

Materials that display adiabatic temperature change or isothermal entropy change when some external stimulus are applied or removed are called solid state caloric materials. These materials are extremely important for new refrigeration technologies that have the potential to replace existing vapor-cycle cooling technologies.

Ferroic materials which have high caloric effects in the vicinity of their ferroic transition regions are known as the most useful caloric materials. These so called ferrocaloric materials are a large family of materials including ferroelectrics, ferromagnetic materials, ferroelastic materials/martensitic shape-memory alloys and multiferroic materials. These materials are exposed to a magnetic field (magnetocaloric effect), electric field (electrocaloric effect), hydrostatic pressure (barocaloric effect), or uniaxial stress (elastocaloric effect). The last two effects are classified as mechanocaloric effect. It is possible to say that the caloric materials are promising when

compared with vapor-compression cooling because all caloric effects that achieve high energy efficiency with low environmental impact.[15] When a magnetic field (ΔH) is applied to a magnetocaloric material, reversible temperature changes occur in the material. In mechanocaloric materials, these reversible thermal changes result from stress field (Δσ) applied to the material while these changes in the electrocaloric materials are caused by the applied electric field (ΔE).[16]

1.3. Properties of Electrocaloric Materials

EC materials are produced in the form of polycrystalline, single crystal, thin and thick film of ceramics. Thin and thick films of polymers are also used in EC materials. Compared to the electrocaloric properties of these forms, the materials in the form of thin and thick film have high EC properties. However, the fact that these materials have volumetric problems for application due to their small size reduces their potential for EC coolers. Single crystals are considered as perfect, defect-free and highly dense. They show relatively large ECE.[6] However, these materials are not suitable for application due to the difficulties in the production and high cost. Thus, research has focused on polycrystals due to the ease of production, characterization and measurements.

Table 1 summarizes the ΔT values of some lead-containing and lead-free materials with their different forms. It is clearly seen that materials with lead-containing have higher ΔT values compared to lead-free materials but under very high electric field. In order to be able to make a more accurate comparison between lead-containing and lead-free materials , the temperature change per unit electric field (ΔT/ΔE) or electrocaloric efficiency should be taken into consideration. The main purpose of researchs on electrocaloric effect is to develop environmentally friendly cooling technology alternatives. Therefore, considering the toxic effects of the lead element, studies on electrocaloric effect are concentrated on lead-free materials.

One of the most commonly investigated materials is $BaTiO_3$ (BT) among the lead-free materials. BT has highly polarisable property and high dielectric strength. These properties make this material a suitable candidate for EC cooling. This material has three structural phase transitions around -80°C, 5°C and 125°C from rhombohedral to orthorhombic, orthorhombic to tetragonal and tetragonal to cubic symmetry with the polar directions <111>, <110> and <001> , respectively.[17]

Table 1.1. The electrocaloric responses of the most important lead-containing and lead-free materials.

Material	T_c (°C)	ΔE (kV/cm)	ΔT (K)	ΔT/ΔE (K.mm/kV)	Method	Ref.
PZT (95/05), thin film	222	776	12	0.15	Indirect	[2]
PZN-PT (92/08), single crystal	180	12	0.23	0.21	Direct	[18]
PMN-PT (92/08), ceramic	23	15	1.4	0.93	Direct	[19]
PMN-PT (85/15), ceramic	17	16	1.7	1.06	Direct	[20]
PMN-PT (75/25), single crystal	100	10	0.61	0.61	Direct	[21]
PMN-PT (65/35), thin film	140	750	31	0.41	Indirect	[22]
P(VDF-TrFE) (55/45), thin film	80	2090	12.6	0.06	Indirect	[23]
$BaTiO_3$, single crystal	129	12	0.9	0.75	Direct	[6]
$BaTiO_3$, ceramic	125	20	1.11	0.56	Indirect	[4]
$BaTi_{0.895}Sn_{0.105}O_3$, ceramic	28	20	0.61	0.31	Indirect	[5]
$Ba_{0.90}Ca_{0.05}Ti_{0.95}Sn_{0.05}O_3$, ceramic	113	10.8	0.53	0.49	Indirect	[24]
$Ba_{0.85}Ca_{0.15}Ti_{0.94}Hf_{0.06}O_3$, ceramic	128	21	0.65	0.31	Indirect	[25]
$Ba_{0.94}Sr_{0.06}Ti_{0.90}Sn_{0.10}O_3$, ceramic	47	15	0.46	0.31	Indirect	[26]
$BaTi_{0.80}Zr_{0.20}O_3$, ceramic	38	21	1.1	0.52	Direct	[8]
$Ba_{0.85}Ca_{0.15}Ti_{0.90}Zr_{0.10}O_3$, ceramic	87	21.5	0.41	0.19	Indirect	[27]

BT has perovskite type crystal structure (ABO_3 structure). The A and B sites are occupied by Ba and Ti elements, respectively. This structure allows doping with different atoms in both the A and B sites. Considering close values of ionic valency and ionic radius of the dopant atom, doping is performed. Therefore distortion of the perovskite structure is relatively small and charge neutrality is conserved. Typical A and B site dopant atoms are given in Figure 1.6. Dopant atoms change the structural phase transition temperatures of BT.

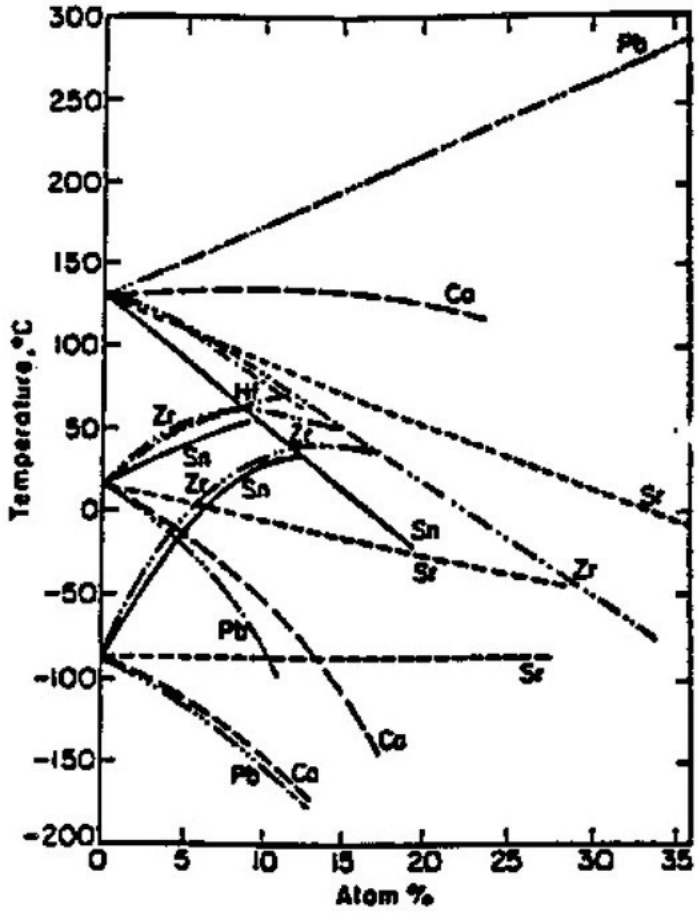

Figure 1.6. The suitable A and B site substitutions for $BaTiO_3$ and their effect on transition temperatures.[17]

Table 1.1 shows the electrocaloric responses from some doped and undoped-$BaTiO_3$ studies including applied electric field and phase transition temperatures of each material. ΔT and ΔT/ΔE values of undoped BT are considerably higher than those of doped-BT. However, doping can be used to decrease the Curie temperature of BT. For applications, a Curie temperature close to room temperature is preferred. Therefore, research has recently focused on doping studies. For example, it is observed that the phase transition temperature at which the ΔT maximum is obtained, reduces from 125°C ($BaTiO_3$) to 28°C ($BaTi_{0.895}Sn_{0.105}O_3$) by doping.

At the moment, EC temperature change (ΔT) values of lead-free materials are not sufficient for use in refrigeration technologies. Therefore, many studies have been conducted to understand the EC properties of materials by developing different doping strategies. With these studies, it is aimed to understand the mechanism that enhances the electrocaloric effect of materials.

1.3.1. Ferroelectric Properties

Ferroelectricity was first discovered in 1921 on Rochelle Salt by Valasek et al. With the discovery of barium titanate ($BaTiO_3$) in 1950's, used for capacitor applications and piezoelectric transducer devices, interest in these materials increased. After $BaTiO_3$, the discovery of many ferroelectrics with perovskite structure such as lead titanate ($PbTiO_3$) accelerated.[28]

In the functional definition, ferroelectrics are known as dielectric materials having spontaneous polarization which can be switched under external electrical field. While the pyroelectrics are known as polar materials having a single symmetry, the ferroelectrics contain two different phases of symmetry as a polar symmetry phase and a high symmetry phase. This is structural definition of ferroelectrics.[29]

Ferroelectric materials possess useful properties such as dielectric, piezoelectric and pyroelectric properties. These materials with high dielectric permittivities are used in capacitors. Due to their high piezoelectric effects, these materials are used in sensors and actuators. They are also used in infra-red detectors due to their high pyroelectric coefficients. These properties classify the ferroelectric materials under the dielectric material class and form the Venn diagram as shown in Figure 1.7 with characteristic features of the materials.

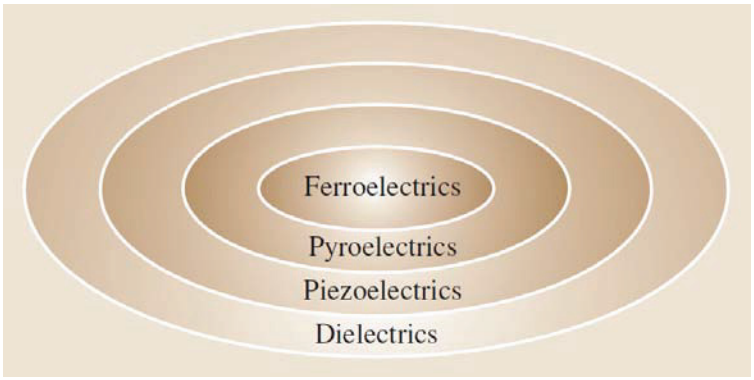

Figure 1.7. Venn diagram showing the relation between dielectrics, piezoelectrics, pyroelectrics and ferroelectrics.[30]

One of the most important characteristics of the ferroelectric materials is that they show ferroelectric hysteresis loop as a result of domain-wall motion under the electric field. Figure 1.8 shows the typical ferroelectric hysteresis loop. Under a low

electric field the polarization increases linearly with the magnitude of the electric field as shown in the AB path. There is no domain switching in the unfavourable direction of polarization because the electric field in this area is not large enough. With the increase of the electric field, the domain switching will start in the direction of the electric field as in the BC path and the measured charge density will also increase. Polarization in this region increases nonlinearly. When all domains under the electrical field are oriented in the same direction as in point C, polarization starts to increase linearly again (CD path). With the reduction of the electric field, some domains switch back, but the polarization under zero electric field is different from zero (point E). The polarization under zero electric field (point E) is called **remanent polarization, P_r**.

To obtain the zero polarization value, the electric field must be reversed as in point F. The electric field at which the polarization is zero is called **coercive field, E_c**. An increase in the opposite direction of the electric field will lead to a new orientation of the dipoles and saturation (point G). To close the loop, the electric field is reversed and reduced to zero.

The **spontaneous polarization**, **P_s** value is obtained from where the intercept of the polarization axis with linear CD path. For polycrystalline materials, it is more accurate to express saturated polarization rather than spontaneous polarization since spontaneous polarization that equals to that of single crystal cannot be obtained in polycrystalline materials.[31]

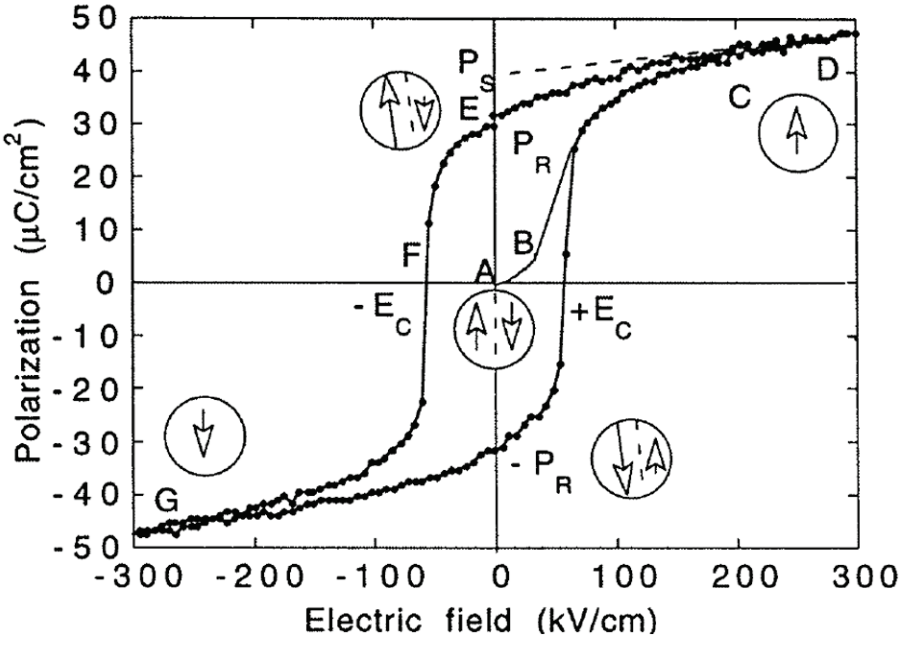

Figure 1.8. Ideal hysteresis loop of a ferroelectric material.[31]

An ideal hysteresis loop should be symmetrical. Therefore, $-P_r = +P_r$ and $+E_c = -E_c$ equations must be provided in the ideal hysteresis loop. Many factors, such as thickness of the sample, charged defects, mechanical stresses, preparation conditions and heat treatment, can change hysteresis loop parameters (P_r, E_c, P_s and shape of the loop).[31]

When the temperature reaches **Curie temperature** (T_c), hyteresis loop becomes slim and linear. This change in the loop demonstrates the phase transition from ferroelectric (low symmetry phase) to the non-ferroelectric or paraelectric phase (high symmetry phase) at T_c.[29]

The temperature dependence of the dielectric constant of the ferroelectric materials is by defined by the Curie-Weiss law[32] shown in Equation 1.1.

$$\varepsilon = \frac{C}{T - T_0} \qquad \textbf{(1.1)}$$

In this equation, T_0 is the Curie Weiss temperature at which temperature begins deviate from linear behaviour. C is the Curie Weiss constant.

Like $BaTiO_3$ introduced above, many ferroelectric materials have perovskite type crystal structure with a chemical formula ABO_3. Most important advantage of this structure is that it allows doping by different atoms in both A and B sites. It is possible to change the phase transition character and the phase transition temperature of ferroelectric materials by dopant atoms.

Doping also causes a change in the Goldschmidt tolerance factor (t) (given in Equation 1.2), which is a measure of the stability of the perovskite structure.[29] In this equation, r_A, r_B and r_O correspond the radii of the atoms at A and B sites and the oxygen atom, respectively.

$$t = \frac{(r_A + r_o)}{\sqrt{2}(r_{B+} r_o)} \qquad \textbf{(1.2)}$$

Doping causes distortion of the crystal structure. Due to this distortion, the bond between the B-site ion and the oxygen ion, which is effective in the emergence of ferroelectric behaviour weakens. This changes the phase transition character of the ferroelectric material from first order to the second order or diffuse character.

Undoped perovskite ferroelectrics have typically first order phase transition. At the phase transition temperature, the dielectric peak maximum increases sharply in a narrow temperature range. In diffuse phase transition, dielectric peak maximum is broadened showing little or no frequency dependence.

The increase in the doping level causes the formation of nanodomains induces **relaxor ferroelectricity**. This behaviour caused by compositional disorder due to doping. This disorder does not disrupt the charge neutrality rule but causes changes in off-center ionic shifts.[29] The most distinctive feature of relaxor ferroelectrics is frequency dependence of the dielectric constant and shifting of the dielectric maximum by frequency.[33]

Relaxors exhibit hysteresis behaviour up to T_m. At T_m, the dielectric maximum shifts to high temperatures with increasing frequency. Relaxor ferroelectrics are subdivided in two groups as ergodic and non-ergodic.[34]

Figure 1.9 (a)-(c) shows the difference between hysteresis, phase transition and dielectric behaviour of normal and relaxor ferroelectrics, respectively. Figure 1.9 (a) shows that coercive field and remanent polarization values of the normal ferroelectrics are typically much higher than relaxor ferroelectrics and a slimmer loop is observed in relaxors.

While normal ferroelectrics such as $BaTiO_3$ have a sharp phase transition at Curie temperature, a broad maximum in dielectric constant is observed at T_m for relaxor ferroelectrics (Figure 1.9 (b)).

Figure 1.9 (c) shows the difference between the dielectric behaviour of normal and relaxor ferroelectrics. As mentioned earlier, the normal ferroelectrics obey the Curie-Weiss law. However, in relaxors, there is a strong deviation from the Curie-Weiss law. A modified Curie-Weiss law given in Equation 1.3 is used to describe the dielectric behaviour of the relaxor ferroelectrics.

$$\frac{1}{\varepsilon} - \frac{1}{\varepsilon_m} = (T - T_m)^{\gamma} \qquad \textbf{(1.3)}$$

In this equation, γ refers to the diffuseness coefficient. While the γ value for normal ferroelectrics is equal to 1, this value approaches to 2 for relaxor ferroelectrics.

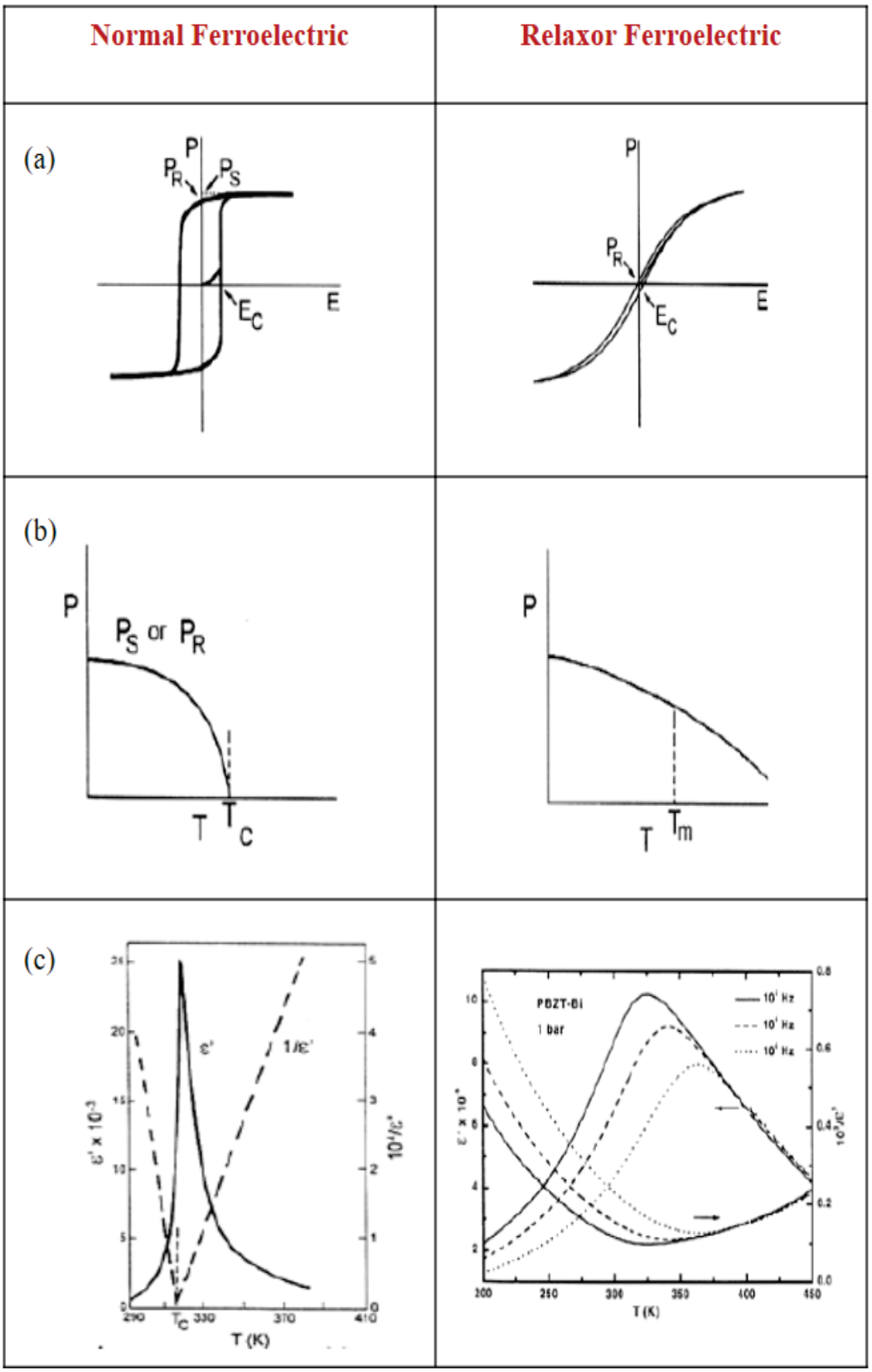

Figure 1.9. Comparison of (a) hyteresis curves (b) phase transition behaviour and (c) dielectric behaviour of the normal ferroelectrics and relaxor ferroelectrics.[35]

1.4. Measurement Methods

In this section, measurement methods of ECE will be explained. ECE can be measured using two different methods as direct and indirect method. In direct measurement, ΔT is obtained from Differential Scanning Calorimetry. It is calculated by using Maxwell equations and ferroelectric hysteresis loops (P-E) in indirect method.

1.4.1. Direct Measurement

The principles of a nonadiabatic scanning calorimeter, expressed by Yao et al., have been used in direct measurements by Luo et al. IR temperature sensor was used to read temperature of sample by comparison the signal with a reference resistor at same voltage. The heater was placed under the EC film which was measured temperature dependence of ECE. For polymer films, a thermistor and a thermal bath were used rather than heater.

In another setup developed by Xiao et al., silicone oil was used to measure the temperature dependence of ECE. Thus, the temperature of the silicone oil and the temperature change value of the EC material under the electric field were read by two thermocouples.

In fact the direct method is not adiabatic. The voltage must be increased rapidly to prevent any heat exchange from the environment. Thus a more accurate measurement can be taken with direct method.[1] Although direct measurement is so seldom and simple method, there are very few studies for measuring the ECE.[7,8,36] The main advantage of this method is that it is more reliable compared to indirect measurement in thin film measurements expected in high EC effect.

1.4.2. Indirect Measurement

The indirect calculation of ECE was first proposed by Thacher in 1968.[37] It was later used to analyze the thin films of PZT by Mischenko et al.[2] The high electrocaloric temperature changes of these thin films accelerated the studies on indirect method. Although there is a scientific discussion about the accuracy of the indirect method, many researchers have adopted this method. The main reason why this method is

popular is that it is difficult to measure directly due to the miniscule caloric effects of thin films.[1] In order to calculate the EC temperature change indirectly, temperature dependent electrical polarization change under constant electric field is needed.

In order to make two different calculations as numerical method and polynomial fit method, the slope of the P-T graphs is needed. For numerical calculation, the slope is calculated using Equation 1.4.

$$\left(\frac{\partial P}{\partial T}\right)_E = \left(\frac{1}{2}\right) * \left(\frac{P_n - P_{n-1}}{T_n - T_{n-1}} + \frac{P_{n+1} - P_n}{T_{n+1} - T_n}\right) \quad \textbf{(1.4)}$$

In the following formulas used for ΔT and ΔS calculations, P represents macroscopic electrical polarization, E_1 (0 kV/cm) and E_2 are initial and final external field, respectively, ρ is density of ceramic, C_p is heat capacity, ΔS is entropy change and ΔT is electrocaloric temperature change.[10]

$$\Delta T = -\frac{T}{\rho C_p} \int_{E_1}^{E_2} \left(\frac{\partial P}{\partial T}\right)_E dE \quad \textbf{(1.5)}$$

$$\Delta S = -\frac{1}{\rho} \int_{E_1}^{E_2} \left(\frac{\partial P}{\partial T}\right)_E dE \quad \textbf{(1.6)}$$

There are some factors that limit the applicability of the indirect method, as in the direct method. It is not correct to calculate the EC temperature change with this method because the non-ergodic relaxor with low relaxation times limits the reproducibility of the indirect method. Also, EC temperature change of materials with only single domain structure is calculated by indirect method and polarization curve must be saturated.[1] Although there are many limitations in the indirect method, this method is preferred by many researchers because it is faster and easier.

1.5. Physical Mechanisms for ECE

In this section, the effect of different physical mechanisms such as first-order and second-order transitions, critical point and relaxor behaviour on ECE will be explained.

1.5.1. First Order vs. Diffuse Phase Transition

Doping of a ferroelectric material affects the EC behaviour by changing the phase transition characteristics. In normal ferroelectric state, phase transition can be of first order or second order (diffuse phase transition). The transition order can be explained by the discontinuity in nth-order derivative of Gibbs free energy at the phase transition temperature. While spontaneous polarization continuously changes for ferroelectric with **second-order phase transition**, spontaneous polarization changes discontinuously (abruptly) for a ferroelectric with **first-order phase transition**.[31] The most significant characteristic of ferroelectrics having first-order phase transition, also known as normal ferroelectrics, is the sharp reduction in polarization with increasing temperature at the phase transition temperature and the $\partial P/\partial T$ ratio increases. Thus ΔT will be large but in narrow temperature range.

Figure 1.10 (a) shows the dielectric and polarization behaviour for ferroelectric with first-order phase transition near T_c. Dielectric behaviour is consistent with the sharp change in polarization. Figure 1.10 (b) shows the continuous decrease in polarization at the Curie temperature.

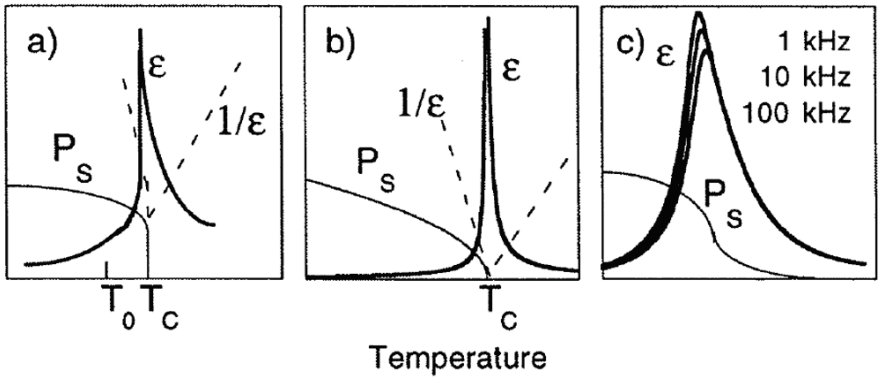

Figure 1.10. Schematic temperature dependence of the dielectric permittivity and spontaneous polarization P_s for a ferroelectric with (a) a first-order and (b) a second-order and (c) for a relaxor ferroelectric.[31]

1.5.2. Critical Point

For $BaTiO_3$, different dopants can be used to change the phase transition temperatures such that a critical point can be obtained in the phase diagram. Since

different ferroelectric phases are present at the critical point, the dielectric constant is high at this point because the material can be polarized along the polarization directions in each of these phases. Thus it is easier to achieve significant polarization change by application of electric field and this leads to greater EC temperature changes. A similar behaviour was observed in the composition closest to the critical point in the $BaHf_xTi_{1-x}O_3$ system.

Dielectric measurements shown in Fig. 1.11 (a) provide a phase diagram for BHT ceramics. The phase diagram in Figure 1.11 (b) shows that x = 0.11 is the critical point and the fact that the dielectric constant has the highest value at this point also supports the above description. At critical point, the electrocaloric effect was 0.35 K under 10 kV/cm electric field. For $BaHf_xTi_{1-x}O_3$ system, this value is the highest electrocaloric effect when compared with other BHT ceramics.[32]

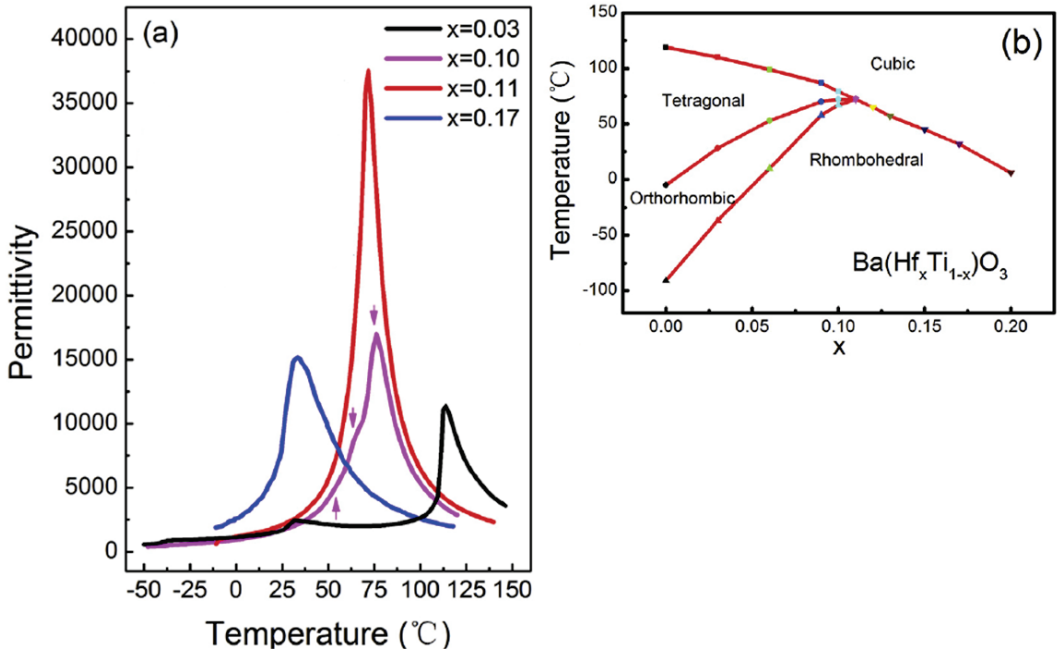

Figure 1.11. (a) Temperature dependence of dielectric constant at 100 Hz and (b) the phase diagram of BHT ceramics.[32]

1.5.3. Relaxors

Ferroelectric relaxors display a diffuse phase transition with a broad maximum in the dielectric permittivity and a strong frequency dispersion of the permittivity below

the temperature of the maximum permittivity as shown in Figure 1.10 (c). Above the temperature of the maximum permittivity, relaxors do not obey the Curie–Weiss law.

As mentioned above, relaxor ferroelectric behaviour is observed when there is compositional disorder due to solid solution formation between different ferroelectric phases or doping of ferroelectrics. The fact that these materials have relatively high ΔT values in a wider temperature range has also increased the interest in these materials. Among the lead-containing ferroelectrics, ΔT value for the most studied PMN ($PbMg_{1/3}Nb_{2/3}O_3$) relaxor composition was found to be 2.5 K under 90 kV/cm electric field at 289 K.[38] Among lead-free ferroelectrics, ΔT value for Zr doped $BaTiO_3$ relaxor composition was found to be 1.1 K under 21 kV/cm electric field at 311 K.[8]

1.6. Motivation of the Thesis

In 2006, the ECE value of PZT ($PbZr_{0.95}Ti_{0.05}O_3$) thin film was measured as 12 K under 776 kV / cm electric field by Mischenko et al. [2] Also this value is high and studies on lead-free bulk materials have accelerated due to low cooling capacity of thin films and limitation of use due to harmful effects of lead-containing materials. Thus works on lead-free ferroelectric ceramic materials have increased. ΔT of $BaTiO_3$, one of the most popular fereoelectric ceramics, was found to be 0.90 K under 12 kV/cm by Moya et al.[6] This value is lower compared to the ΔT value of PZT, however ΔT obtained per applied electric field (ΔT/ΔE: electrocaloric efficiency) was found to be larger for $BaTiO_3$. This ΔT is however obtained only over narrow range of temperatures around T_c of $BaTiO_3$ due to first order nature of the ferroelectric phase transition. In order to extend the temperature range, tune T_c, and make use of other mechanism to obtain large ΔT, different studies have been carried out by substituting different elements to the A and B sites of $BaTiO_3$.

Aim of this study was to investigate the EC properties of the $Ba_{0.8}Sr_{0.2}Ti_{1-x}Z_xO_3$ system for $0 \leq x \leq 0.10$, whose dielectric and pyroelectric properties had previously been studied by Szymczak et al.[39] Szymczak obtained a phase diagram as shown in Figure 1.12 (b) by using the dielectric constant measurements in Figure 1.12 (a) for different compositions. The main motivation of this study was to investigate how ECE changes in different regions of this phase diagram. In this context, it was decided to study the EC properties of five different compositions using the following phase

diagram. The composition of undoped BST and $BSTZ_{0.03}$ which were thought to be dominated by the first order phase transition were selected. To determine the EC behaviour in the critical region, $BSTZ_{0.05}$ and $BSTZ_{0.07}$ compositions were selected while $BSTZ_{0.10}$ which is considered to show diffuse phase transition, was also included in the study.

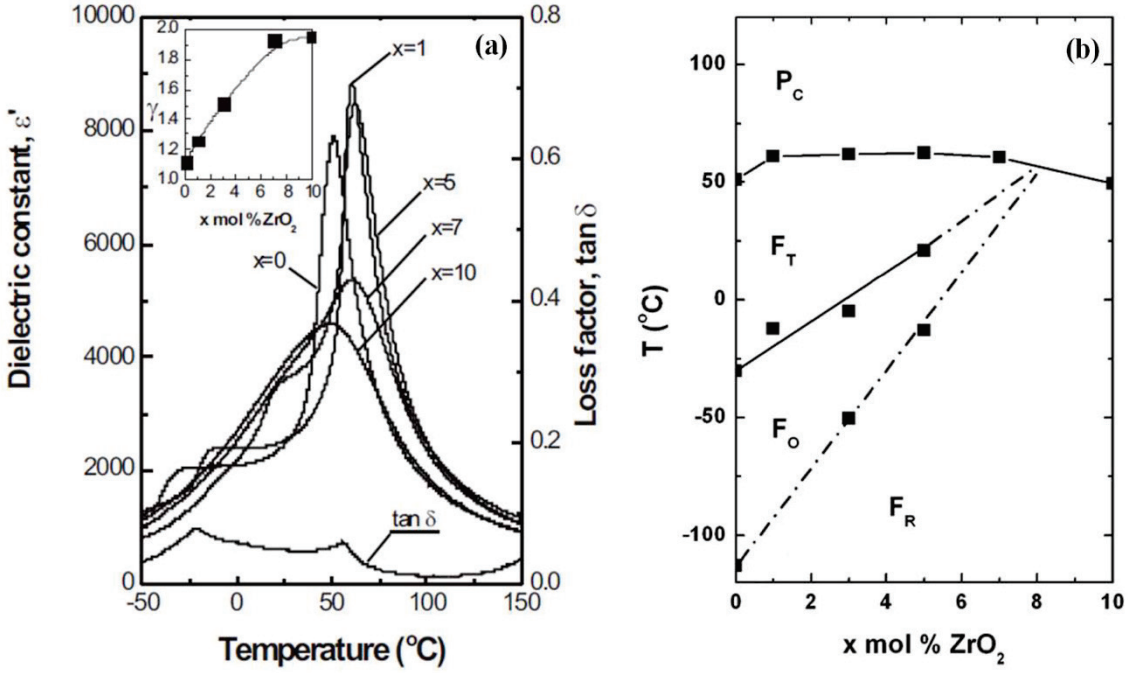

Figure 1.12. (a) Dielectric constant values for $BSTZ_x$ ceramics ($0 \leq x \leq 0.10$) and dielectric loss for x=0.01 as a function of temperature at 1 kHz. Inset shows diffuseness exponent, γ and Zr content. (b) Temperature-Composition (T-x) phase diagram of $BSTZ_x$ ceramics for $0 \leq x \leq 0.10$.[39]

These different compositions at different points of the phase diagram, have different phase transition characteristics and therefore are known to activate different mechanisms of the electrocaloric effect. Even though there are reports on electrocaloric effect of Sr doped $BaTiO_3$ in the literature[7,40,41], electrocaloric properties of Sr and Zr co-doped ceramics of different Zr content has not been reported.

CHAPTER 2

EXPERIMENTAL METHODS

2.1. Material Preparation

In this section, the synthesis method of $BSTZ_x$ ceramics for $0 \leq x \leq 0.10$ is explained in detail. Figure 2.1 illustrates the flow chart of the synthesis. $BSTZ_x$ (x=0.00, 0.03, 0.05, 0.07 and 0.10) bulk ceramics were prepared by conventional solid state reaction method using barium carbonate ($BaCO_3$, >99.9%), titanium dioxide (TiO_2, ≥99.9%), strontium carbonate ($SrCO_3$, >99.9%), and zirconium oxide (ZrO_2, >99.9%) as raw materials.

Firstly, the starting powders were dried in order to remove chemically bound water at 200°C for 12 hours. Therefore, the powders were weighed in stoichiometric ratios. After weighing, the starting powders were milled in 30 ml nalgene container with pure ethanol and zirconia balls for 12 h using a ball-mill. The mass ratio (ball-to-powder) was 10:1. After mixing, the suspension was dried at 78.5°C for 12 h in order to evaporate ethanol and then dried powders were calcined at 1100°C for 4 h.

The calcined powders were mixed with 2wt% polyvinyl alcohol (PVA) as a binder in pure water for 8 h. Then, pure water was evaporated from the mixture in a controlled manner and the powders were ground in an agate mortar. The powders were pressed into 10 mm-diameter pellets at 375 MPa by hydraulic press and then these pellets were sintered at 1400°C for 4 h in a alumina crucible. For microstructural analysis and electrical measurements, these ceramics were polished to 1 mm thickness by using sand papers 600, 1000 and 2000 mesh in order.

2.2. Characterization of the Materials

In this section, some analyses were done for the characterization of synthesized ceramics.

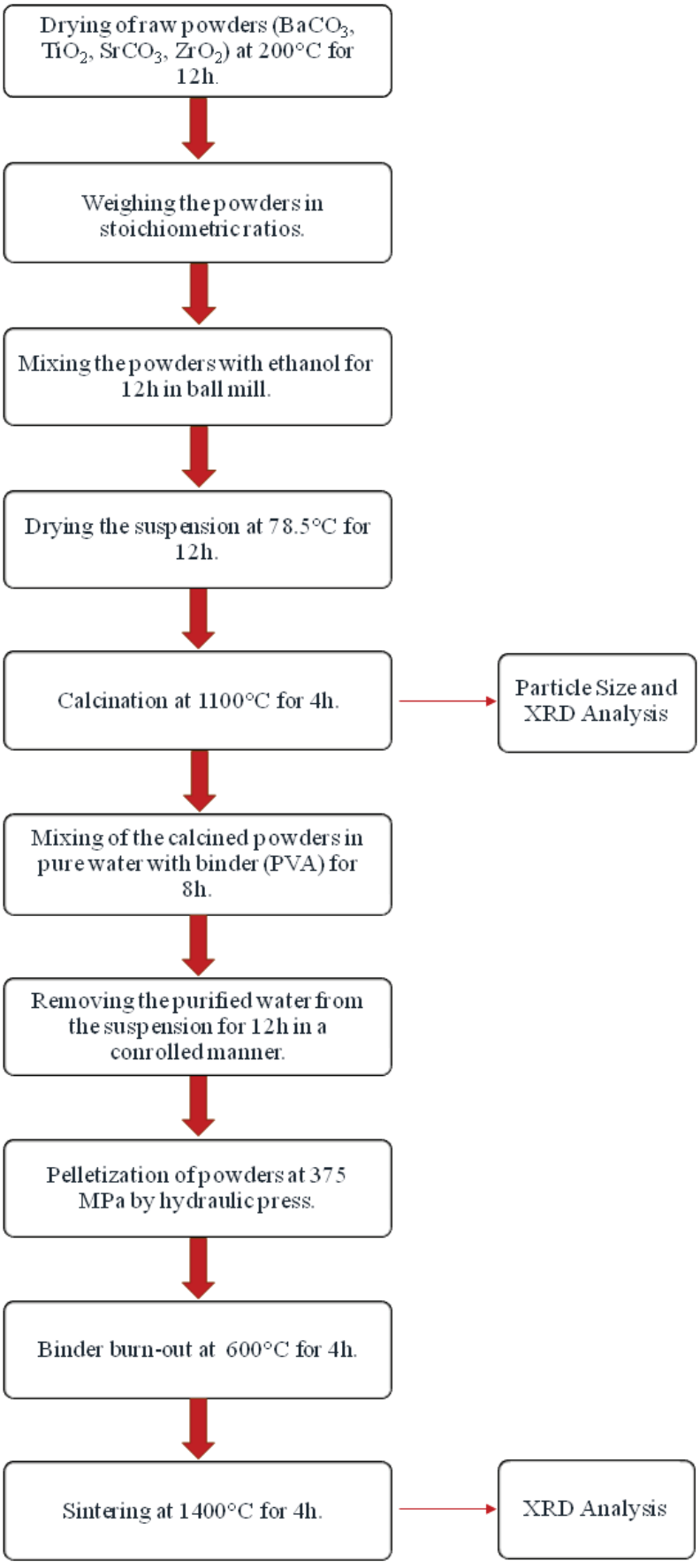

Figure 2.1. Flow chart of the synthesis.

2.2.1. Particle Size Analysis

In this study, Dynamic Light Scattering (DLS) technique was used for particle size analysis of the powders after calcination. This technique that is also known as Photon Correlation Spectroscopy (PCS) or Quasi-Elastic Light Scattering (QELS) is a very useful analytical method for determining the size distribution of particles in suspension. One of the most important advantages of this technique is that it allows to perform analysis in a wide size range from below 0.005 μm to several microns.

In this study, particle size analysis of the powders after calcination was performed with the Zetasizer Nano ZS (Malvern Instruments, Worcestershire,UK) at the Materials Science and Engineering department in IZTECH. For each composition, 5 mg of the powder was dispersed with 1.5 ml of ethanol in a cuvette. The measurement time of the prepared suspension is about 5 minutes.

2.2.2. Phase Analysis

X-ray Diffraction (or XRD) is used for doing phase analysis of the samples. The general working principle of this method is based on the similarity between the wavelength of the X-ray lights and the interatomic distance (1 Å).[42]

Phase analysis of the powders obtained after calcination and sintering processes was performed with a X-ray Diffractometer (XRD) instrument (Philips X'Pert Pro, equipped with Cu Kα source) at Materials Research Center in IZTECH. XRD patterns were collected between 20° and 80° with 0.0170 (°2Θ) step size and 56.3 seconds per step. X-ray patterns as shown in the Results and Discussion section were analyzed with the search and match function of the High Score Plus program.[43]

2.2.3. Microstructural Analysis

Microstructural analysis and grain size determination of the synthesized samples were done by Scanning Electron Microscope (SEM).

Thermal etching is generally necessary to obtain a clear SEM image from sintered and polished ceramic samples. The etching temperature is generally known to be 100°C below the sintering temperature for ceramic samples. It is not possible to see

grain boundaries without thermal etching because polishing process makes grain boundaries invisible. Due to thermal etching, a contrast is formed between the grain and grain boundaries.[44]

In this study, the sintered and polished ceramics were thermally etched at 1300°C for 1 hour. Then, the ceramic samples were ultrasonically disaggregated in pure acetone and dried at 100°C for 12 hours to remove humidity. The SEM instrument used is a Philips XL 30S FEG with an EDX (Energy Dispersive X-Rays) detector at the Materials Research Center in IZTECH. Both Secondary Electron and Back Scattering Detectors (BSD) were used to obtain SEM images. However, only BSD images showing larger contrast between grains and grain boundaries are included in this thesis. The working principle of BSD is based on the differences in the number of atoms (Z) in the sample. Larger atoms are more powerful electron scatterers than light atoms. This difference between atomic numbers makes it easier to distinguish between different phases.

EDX analysis was also performed to check the composition of the samples however due to the overlapping X-ray energies of Ba and Ti the composition cannot be accurately determined. Therefore EDX results are not included in this thesis.

2.2.4. Density Measurements

Accurate density measurement is important since density affects the dielectric breakdown strength of the samples and other physical properties for ECE. Archimedes' principle is used for the density measurements of the samples. Following density equation is used to estimate the density.

$$\mathrm{p} = \frac{M_{dw}}{M - M_{ww}} * \mathrm{p}_w \qquad \textbf{(2.1)}$$

In this equation, p and p_w represent density values of ceramic sample and water (p_w= 1.0 g/cm^3) respectively. M_{dw} is dry weight of the ceramic and M_{ww} is weight of the ceramic in water. M corresponds to the weight of the ceramic after removed from the water. The measurements required for the density estimation were done using the density kit of the Radwag-As 220.R2 analytical balance.

2.3. Electrical Measurements

In order to characterize the electrocaloric properties of the samples, temperature dependence of dielectric and ferroelectric properties was measured. For both electrical measurements, the thickness and diameter values of the sintered and polished ceramics were recorded. Typically pellets with 8 mm diameter and less than 1 mm thickness were used. Silver epoxy was coated onto the surfaces of the pellets to form conductive electrodes. Silver epoxy is cured by firing at 135°C for 7 min. The pellets were placed in the sample holder as shown in Figure 2.2 for the measurements. The sample holder was filled with insulating silicone oil for preventing electrical sparks.

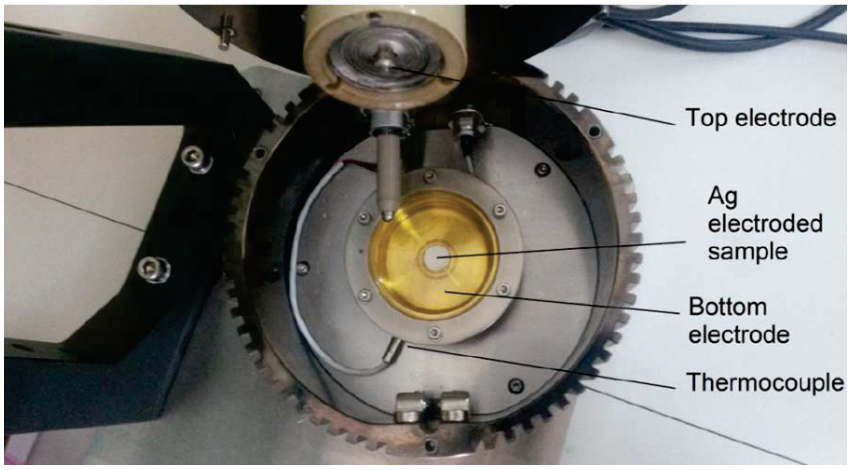

Figure 2.2. Sample holder used in electrical measurements.

2.3.1. Dielectric Constant Measurements

In this study, dielectric measurements were done for determining phase transition behaviour and Curie temperatures of the ceramics and also for constructing the phase diagram. Dielectric materials are known as insulating or nonmetallic materials. The separation of positive and negative electrically charges on an atomic or molecular level under the electric field makes these materials useful for capacitor applications.

The dielectric constant or relative dielectric constant, ε_r is a measure of charge storage capacity and can be calculated using the parallel plate capacitor equation given in Equation 2.2.

$$\varepsilon_r = \frac{C.l}{A.\varepsilon_0} \quad \textbf{(2.2)}$$

where A is the area of the plates, l is the thickness of the pellets, ε_0 is the dielectric constant of vacuum and ε_r is the relative dielectric constant of the dielectric material.[45]

Capacitance measurements were performed every 3°C in the temperature range between 24°C and 200°C by Keysight E4980AL Precision LCR-meter at Electroceramics Laboratory at IZTECH. Temperature is controlled by the temperature controller of the Aixacct ferroelectric test system. Ac signal with 1 V potential is applied to the pellets at different frequencies (120 Hz, 1 kHz, 10 kHz and 100 kHz) and capacitance and dielectric loss values are recorded. Dielectric constant was calculated from the Equation (2.2) by using the capacitance values.

2.3.2. Polarization Measurements

In order to characterize ferroelectric properties and calculate electrocaloric effect (ECE) using indirect method, P-E loop or hysteresis loop measurements were performed every 3°C in the temperature range between 24°C and 108°C with an Aixacct TF Analyzer 1000 unit connected with a 10 kV high-voltage amplifier (TREK Model 610E) at the Electroceramics Laboratory at IZTECH.

Temperature-dependent hysteresis loops of ceramic samples were obtained at 1 Hz. The temperature range of measurement was determined by considering the Curie temperatures of the ceramics. The measurements for all ceramics continued until hysteresis loops became completely linear, showing paraelectric character.

CHAPTER 3

RESULTS AND DISCUSSION

3.1. Phase Analysis

Phase analysis of the synthesized samples as described in the material preparation section was done after each heat treatment (calcination and sintering) process by X-ray diffraction (XRD) experiments. Figure 3.1 (a) shows the room temperature XRD patterns performed on $BSTZ_x$ calcined samples in the range of 20° to 80° and Figure 3.1 (b) shows close examination of Bragg peak between 43°-48° as a function of x.

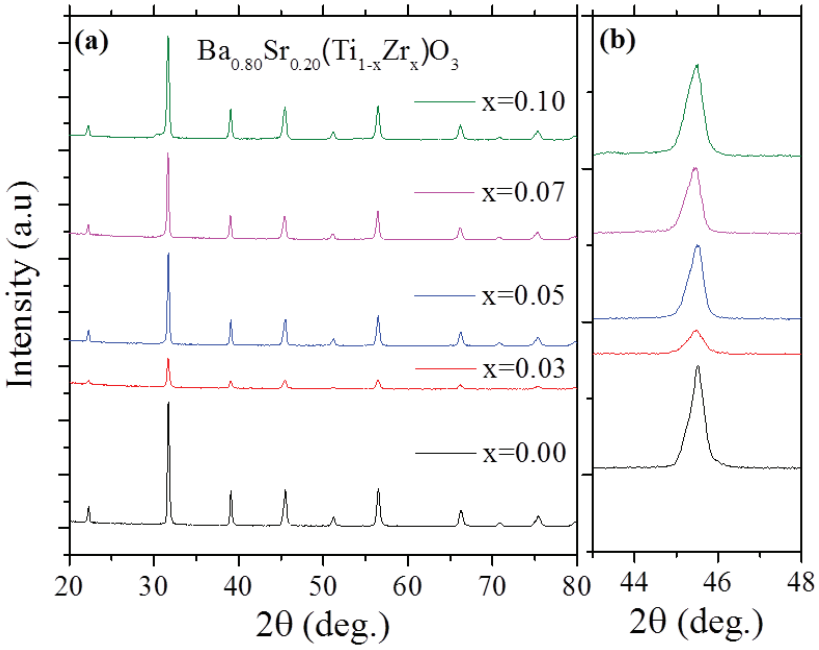

Figure 3.1. XRD patterns of calcined $BSTZ_x$ samples for $0 \leq x \leq 0.10$ in the range of 2Θ (a) from 20° to 80° and (b) close examination between 43°-48°.

It can be seen that the phases are not completely formed after calcination process. The calcination process is a heat treatment reaction that allows the decomposition of carbonates. Therefore, a single calcination process may not always be sufficient to achieve a homogeneous single phase.

Figure 3.2 (a) indicates the room temperature XRD patterns performed on sintered $BSTZ_x$ samples for $0 \leq x \leq 0.10$ in the range of 20° to 80° and Figure 3.2 (b) shows close examination of the range between 43°-48°.

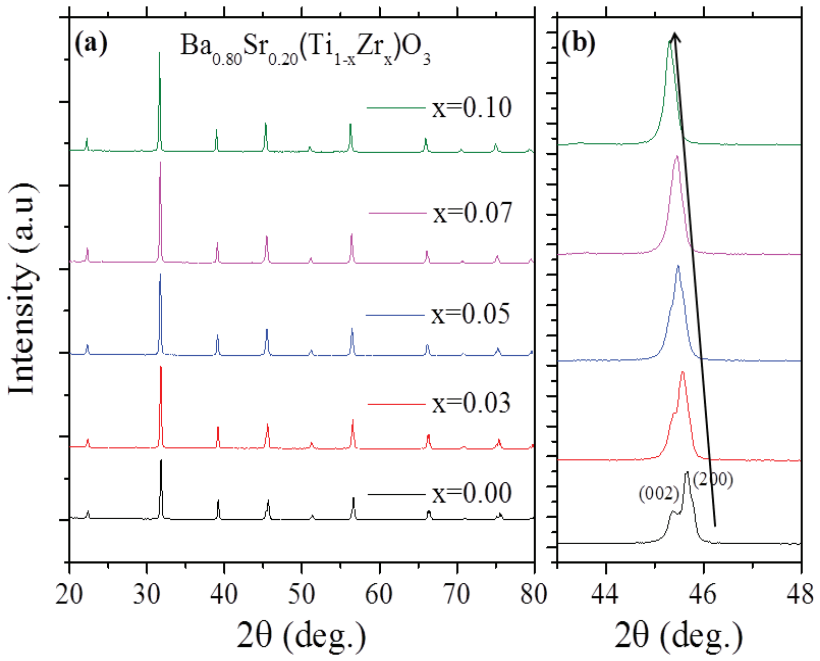

Figure 3.2. XRD patterns of sintered $BSTZ_x$ samples for $0 \leq x \leq 0.10$ in the range of 2Θ (a) from 20° to 80° and (b) close examination between 43°-48°.

Peak splitting near 45° corresponds to the tetragonal phase in the perovskite structures. In order to identify the symmetry of the phases, a close examination is required in this region. All these ceramics have a pure perovskite phase without secondary impurity phases. Due to the diffusion of Zr element into the crystal structure, change in lattice parameters causes gradual overlapping of two diffraction peaks and peak shifting around 46°. With the increase of the Zr substitution, it can be seen that the peak around 46° is shifting towards the lower angles. This change could be explained by the fact that Zr^{4+} ion has a larger ionic radius than Ti^{4+} ion (0.72 Å and 0.605 Å, respectively).[46]

It is observed that the tetragonality has disappeared with the increase of Zr amount. Due to the splitting of (002) and (200) diffraction peaks, tetragonal symmetry can be deduced for undoped BST and x=0.03 ceramics. Zr-doped with x=0.05 ceramic is between orthorhombic and tetragonal region according to the phase diagram in the literature[39] and so it is expected that peak splitting is not clear as observed in Figure 3.2

(b). x=0.07 and x=0.10 ceramics are in the rhombohedral phase region at room temperature and the absence of peak splitting is consistent with rhombohedral symmetry.

3.2. Particle Size Analysis

Particle size analysis of the powders after calcination process was done by Dynamic Light Scattering (DLS).

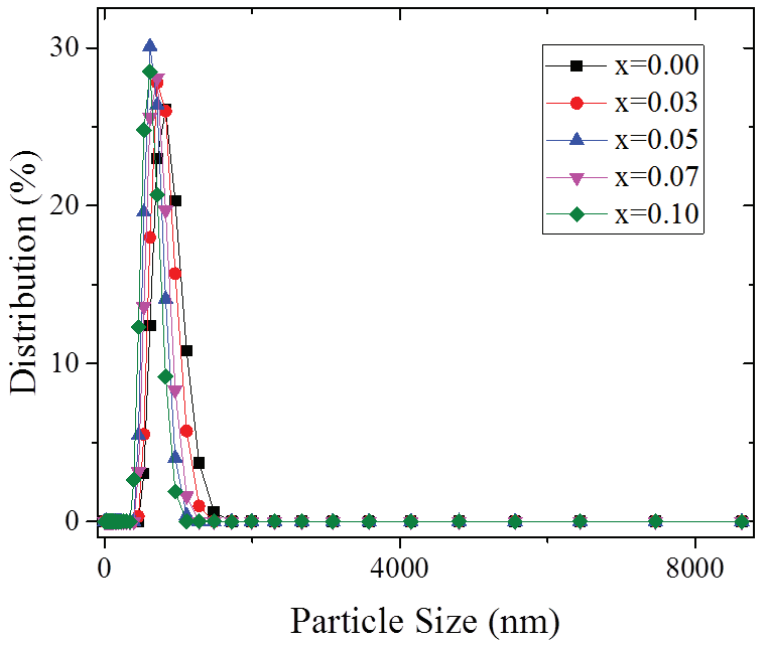

Figure 3.3. Particle size distribution for $BSTZ_x$ samples after calcination.

Particle size distribution is homogeneous without an extra peak for each composition as shown in Figure 3.3. Thanks to this homogenous distribution, sintering is expected to be more effective. The average particle sizes of these compositions are 825, 712, 615, 712 and 615 nm for x=0.00, 0.03, 0.05, 0.07 and 0.10, respectively. The fact that these values are close to each other proves that the density values as described in Table 3.1 do not change much between compositions. % theoretical density was expressed with respect to the theoretical density of undoped BST composition (5.83 g/cm^3) using and the following Equation (3.1).

$$\%\, density = \frac{d_{experimental}}{d_{theoretical}} * 100 \qquad \textbf{(3.1)}$$

Table 3.1. Density values of sintered $BSTZ_x$ samples for $0 \leq x \leq 0.10$.

Compositions	d (g/cm^3)
$Ba_{0.8}Sr_{0.2}TiO_3$	5.23 (90%)
$Ba_{0.8}Sr_{0.2}Ti_{0.97}Zr_{0.03}O_3$	5.33 (91%)
$Ba_{0.8}Sr_{0.2}Ti_{0.95}Zr_{0.05}O_3$	5.36 (92%)
$Ba_{0.8}Sr_{0.2}Ti_{0.93}Zr_{0.07}O_3$	5.35 (92%)
$Ba_{0.8}Sr_{0.2}Ti_{0.90}Zr_{0.10}O_3$	5.33 (91%)

Particle size and density values could be correlated with each other to verify the effect of particle size on sintering process. It could be said that decreasing particle size facilitates diffusion kinetics of the compositions throughout sintering process and consequently density increases with the decrease of particle size.

3.3. Microstructural Analysis

Microstructural analysis of the thermally etched $BSTZ_x$ ceramics for $0 \leq x \leq 0.10$ was done by Scanning Electron Microscopy (SEM). Figure 3.4 (a)-(e) shows the microstructure and also grain size of the sintered ceramics at 1400°C.

All ceramics have dense microstructures and are practically non-porous. It is observed that Zr substitution increases the grain size. Grain sizes are approximately 30.2, 36.3, 68, 77.6 and 96 μm for x=0.00, 0.03, 0.05, 0.07 and x=0.10, respectively. However, an impurity phase, which was not detected in XRD experiments, was observed for all compositions between the grain boundaries.

Energy-Dispersive X-ray Spectroscopy (EDX or EDS) analysis for the characterization of the impurity phase was done but X-ray energy values of Ba and Ti elements are very close to each other. In addition, X-ray energy values of Sr and Zr elements are too close to each other as shown in Table 3.2. EDX analysis gives no clear information about the compositions and phases for this study. Due to low amount of the impurity phase (no impurity phase was visible in XRD plots) we assume that the impurity phase does not affect the electrical measurements.

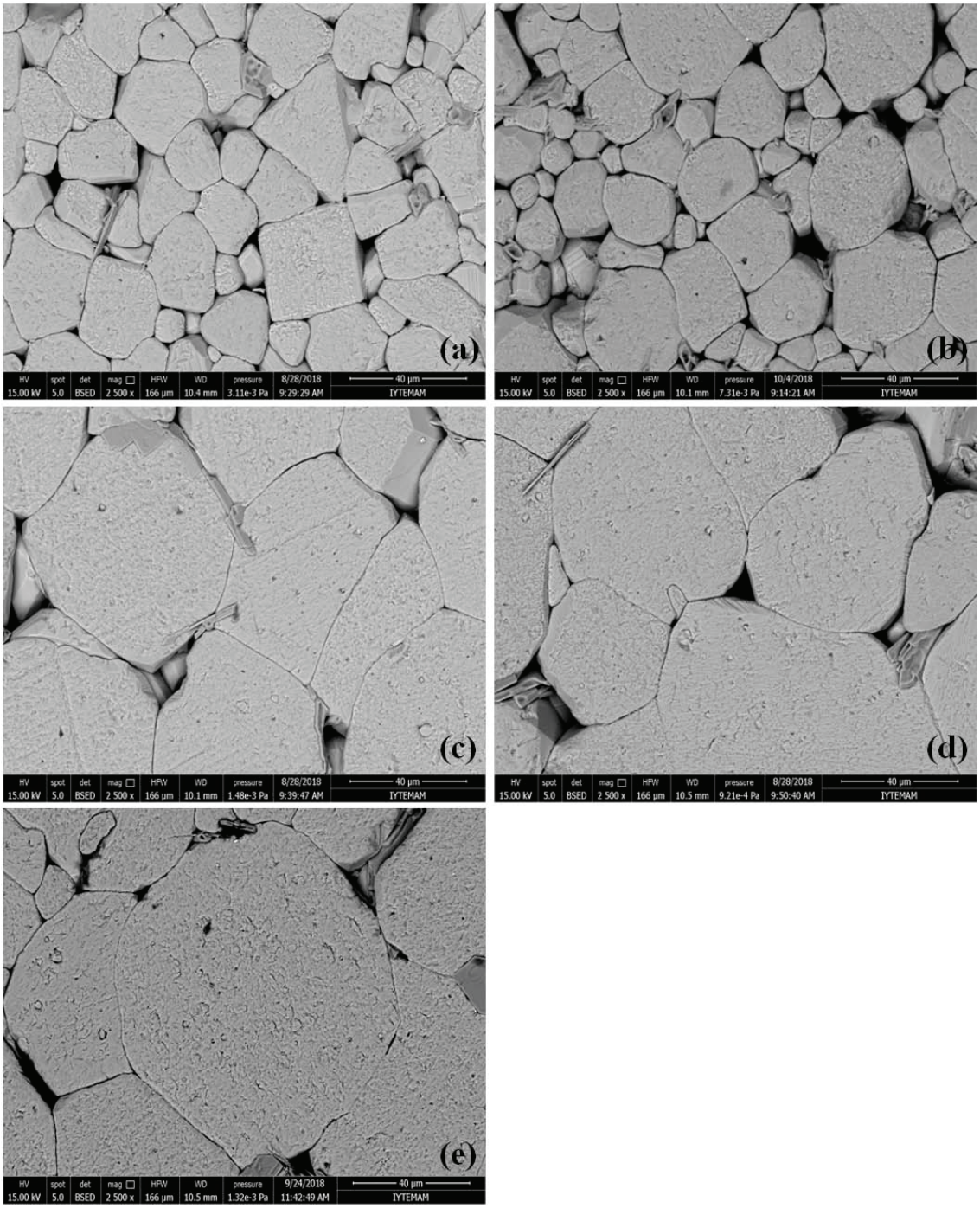

Figure 3.4. SEM micrographs of $BSTZ_x$ ceramics for (a) x=0, (b) x=0.03, (c) x=0.05, (d) x=0.07, and (e) x=0.10.

Since the sintering temperature is the same for each composition, different amounts of Zr substitution on the B-site of the perovskite structure should be responsible from the changes in the grain size. Zr substitution increases the grain size in agreement with the literature.[46]

Table 3.2. X-ray energies of Ba, Ti, Zr and Sr elements.[47]

Z	Element	Kα1	Kβ1	Lα1	Lβ1
56	Ba	32.194	36.378	**4.466**	**4.828**
22	Ti	**4.512**	**4.933**	0.452	0.458
40	Zr	**15.775**	**17.668**	2.044	2.126
38	Sr	**14.165**	**15.835**	1.806	1.871

3.4. Dielectric Measurements

Capacitance and dielectric loss values for each composition were measured between 24°C and 200°C with the LCR meter. Dielectric constant was calculated by using these values as described in the Section 2.3.1.

Figure 3.5 (a)-(e) shows the dielectric constant values for each ceramic sample at different frequencies. For the undoped (x=0) BST ceramic in the Figure 3.5 (a), the sharpness of dielectric peak behaviour shows that there is a first order phase transition at 69°C (Curie temperature or T_c) and this behaviour is consistent with studies in the literature.[48,49]

The behaviour did not change much for x = 0.03 and x = 0.05 and it was observed that T_c decreased slightly with the addition of Zr. T_c values are 64°C and 63°C for x=0.03 and x=0.05, respectively. For the x = 0.07 composition, the dielectric peak maximum becomes sharper and T_c decreases to 60°C as shown in Figure 3.5 (d).

There is also an extra peak around 33°C. x=0.10 sample shows the broadest dielectric peak however peak maximum does not shift to higher temperatures with increasing frequency ruling out relaxor behaviour as shown in Figure 3.5 (e). There is also a significant decrease in Curie temperature (53°C) in comparison with the other compositions.

Figure 3.6 (a) shows the dielectric constant values measured at 1 kHz for all compositions. When dielectric constant and loss values in Figure 3.6 (a)-(b) are examined, it is clear that T_c and the sharpness of dielectric peak decreases with the Zr substitution, implying that the dielectric behaviour changes from the first order phase transition to the diffuse phase transition. It can be observed that the dielectric constant is

the highest for the x = 0.07 composition. In addition, Figure 3.6 (b) shows the dielectric loss of $BSTZ_x$ ceramics which is consistent with dielectric behaviour.

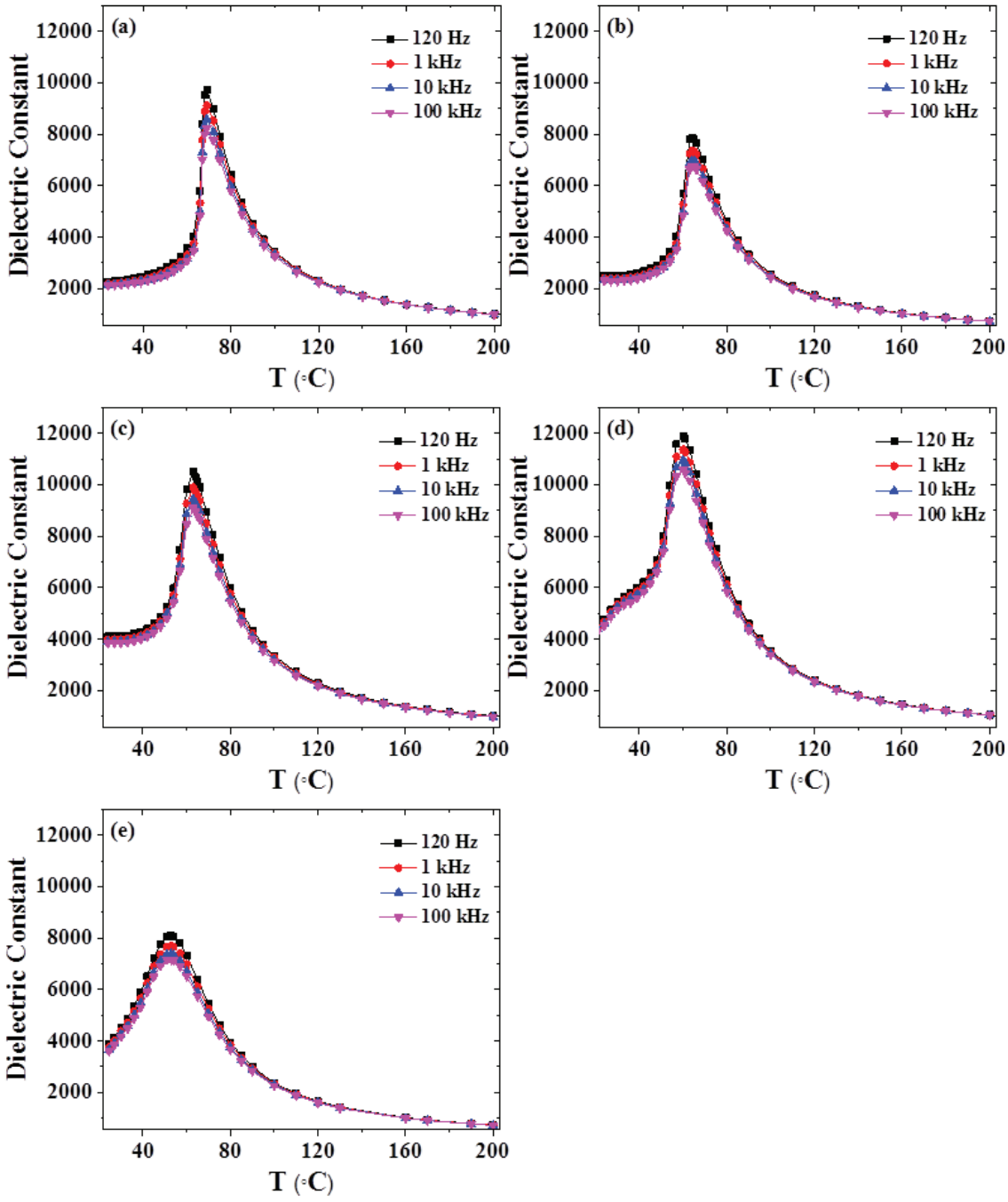

Figure 3.5. Temperature dependence of dielectric constant of $BSTZ_x$ ceramics for (a) x=0, (b) x=0.03, (c) x=0.05, (d) x=0.07, and (e) x=0.10.

The diffuseness constant (γ) values, of the samples were calculated by using the dielectric constant versus temperature plots. Normal ferroelectrics follow the linear behaviour of Curie-Weiss law above Curie temperature, T_c. In diffuse phase transition, a

deviation from Curie-Weiss law above T_c occurs because of a broadening of the maximum dielectric constant near T_c.

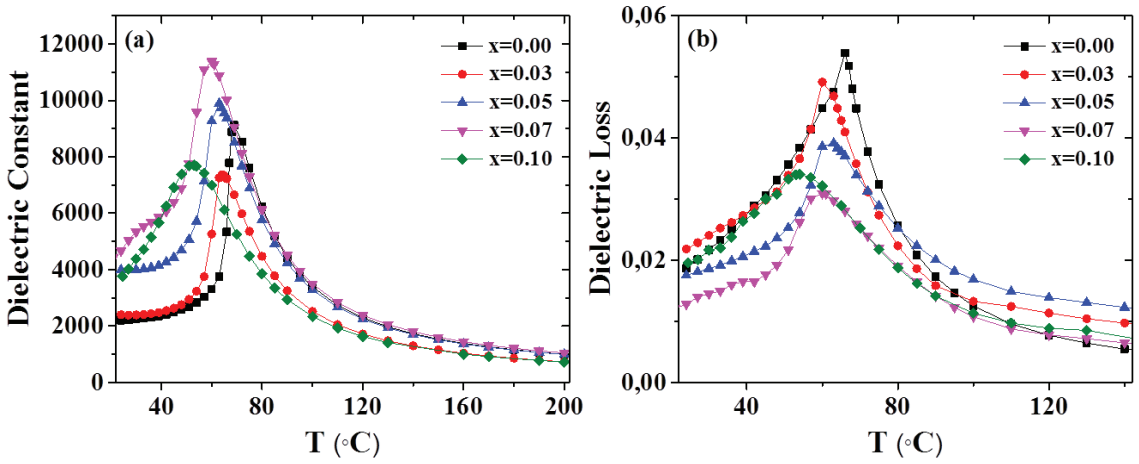

Figure 3.6. Temperature dependence of dielectric constant (a) and dielectric loss (b) at 1 kHz for the $BSTZ_x$ ceramics with x=0, x=0.03, x=0.05, x=0.07, and x=0.10.

To determine the diffuseness of a phase transition, modified Curie-Weiss law expressed in Equation 3.2 is used. In this equation, ε_r corresponds to the maximum dielectric constant, T_m is the temperature at which the maximum dielectric constant is observed and γ and C' are assumed as constants. $\gamma = 1$ describes normal ferroelectric behaviour while $\gamma = 2$ suggests complete transition to a relaxor behaviour.[50]

$$\frac{1}{\varepsilon} - \frac{1}{\varepsilon_m} = \frac{(T - T_m)^{\gamma}}{C'} \qquad \textbf{(3.2)}$$

The diffuseness constant, γ of undoped BST ceramic was calculated as shown in Figure 3.7. Firstly, the T_m and T_{cw} temperatures were determined as shown in Figure 3.7 (a) by fitting the temperature-dependent inverse dielectric constant graph with a linear equation (solid line). T_{cw} temperature was accepted as the temperature at which experimental data (square symbols) begins deviate from linear behaviour. Then γ coefficient was obtained from the slope of the graph in Figure 3.7 (b). The same procedure was repeated for other compositions with Zr addition and γ values was found as 1.143, 1.162, 1.202, 1.247 and 1.326 for x=0.00, 0.03, 0.05, 0.07 and x=0.10, respectively. The value of diffuseness constant increases with the increase of Zr addition as shown in Figure 3.8.

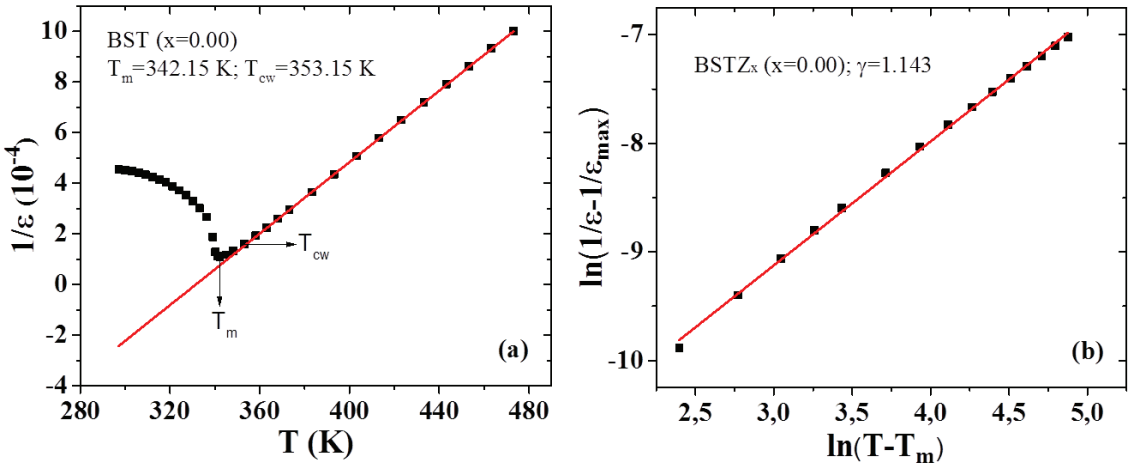

Figure 3.7. The inverse dielectric constant plotted at 1 kHz as a function of temperature (a) and the double logarithmic plot to deduce diffuseness constant, γ (b) for undoped BST ceramic (the square symbols denote the experimental data and the solid line denotes the linear fits using the Curie-Weiss law).

Although the highest value is obtained for x=0.10, the γ value for this composition is much smaller than the value for the relaxor behaviour (γ =2). Large amount of B site doping strengthens the relaxor behaviour.[25,36] However in this study the B site doping is not sufficient for inducing relaxor behaviour consistent with some literature studies.[32,50]

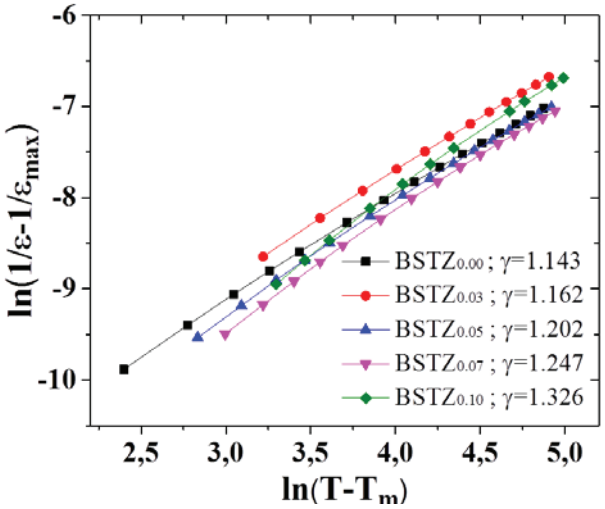

Figure 3.8. Diffuseness constants (γ) of $BSTZ_x$ ceramics.

Figure 3.9 shows the phase diagram of $BSTZ_x$ ceramic systems for $0 \leq x \leq 0.10$ which is constructed by using the temperature-dependent dielectric constant data of the

$BSTZ_x$ ($0 \leq x \leq 0.10$) and dielectric data of Szymczak et al. Black symbols are data points of the phase transition temperatures from the reference study[39] and red symbols are data points of the phase transition temperatures from this study. In this study, the phase diagram could not be completely constructed because the dielectric measurement range is between 24°C and 200°C. However, when ferroelectric-paraelectric phase transition temperatures (T_c values) are examined, the phase transition temperatures are similar to those of Szymczak et al.

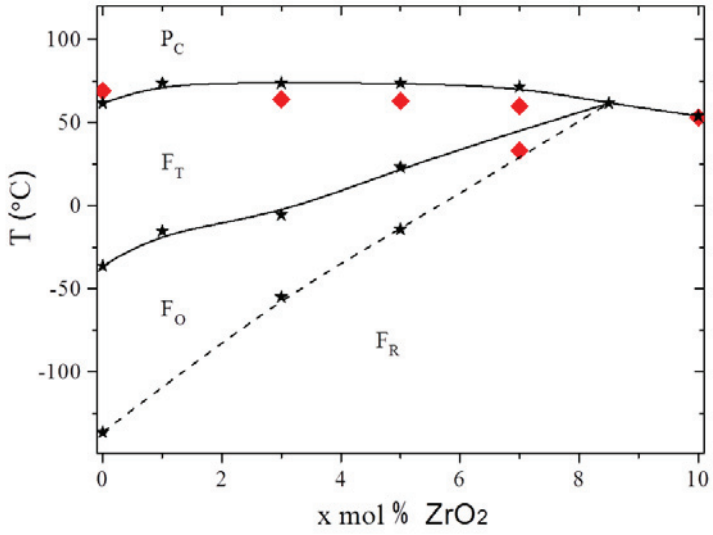

Figure 3.9. Phase diagram of $BSTZ_x$ ceramics for $0 \leq x \leq 0.10$; black symbols are data points of the phase transition temperatures from the reference study[39] and red symbols are data points of the phase transition temperatures determined using dielectric measurements in this study.

According to the phase diagram, T_c decreases while tetragonal-orthorhombic phase transition temperatures (T_{T-O}) and orthorhombic-rhombohedral phase transition temperatures (T_{O-R}) increase as the Zr doping level x rises. Thus, the phase transition temperatures become close to each other with Zr substitution. Highest dielectric constant value for x=0.07 sample can be explained by the fact that this composition is in the critical region where more than one ferroelectric phase is present because the material can be polarized along the polarization directions in each of these phases. Looking at the phase diagram, it can also be said that the extra peak which is around 33°C for this composition corresponds to the orthorhombic-tetragonal phase transition temperature.

In summary, it is known that the Curie temperature decreases with the addition of Zr. In fact, the addition of Zr weakens the bond between the Ti and the O ions. Since this bond is weak, the Ti ion is able to maintain its tetragonal position only at low temperatures. Therefore, with the addition of Zr, T_c shifts to lower temperatures.[46] The fact that T_c is around room temperature is one of the main motivations of this study.

3.5. Polarization Measurements

Ferroelectric hysteresis loops (P-E) were measured every 3°C on heating in the temperature range of interest under different electric fields by using Aixacct TF1000 instrument in order to evaluate the electrocaloric effect (ECE) of all compositions.

Figure 3.10 (a)-(e) displays the P-E hysteresis loops of $BSTZ_x$ ceramics for $0 \leq x \leq 0.10$ at five different temperatures and at 1 Hz. The curves show that the saturation polarization, coercive field and remnant polarization gradually decrease as the temperature increases. All compositions are ferroelectric below the Curie temperature. When the temperature is higher than the Curie temperature, the P-E loops become slim and linear. This change in the P-E loops demonstrates the phase transition from ferroelectric to the paraelectric phase.[25]

Figure 3.10 (f) shows the comparison of all compositions at 24°C and 1 Hz. The saturation was reached for each ceramic under 20 kV/cm electrical field at this temperature and ferroelectric behaviour is clear for all samples. Table 3.3 summarizes the P_s, P_r as well as E_c under 20 kV/cm at 24°C and 1 Hz. The P_r, P_s and E_c values of the undoped BST ceramic are higher than others.

Table 3.3. Hysteresis loop parameters of the $BSTZ_x$ ceramics.

Composition	P_s ($\mu C/cm^2$)	P_r ($\mu C/cm^2$)	E_c (kV/cm)
$Ba_{0.8}Sr_{0.2}TiO_3$	16.37	8.84	1.71
$Ba_{0.8}Sr_{0.2}Ti_{0.97}Zr_{0.03}O_3$	12.67	5.94	1.66
$Ba_{0.8}Sr_{0.2}Ti_{0.95}Zr_{0.05}O_3$	14.06	6.83	1.69
$Ba_{0.8}Sr_{0.2}Ti_{0.93}Zr_{0.07}O_3$	14.49	6.45	1.27
$Ba_{0.8}Sr_{0.2}Ti_{0.90}Zr_{0.10}O_3$	12.96	4.40	1.08

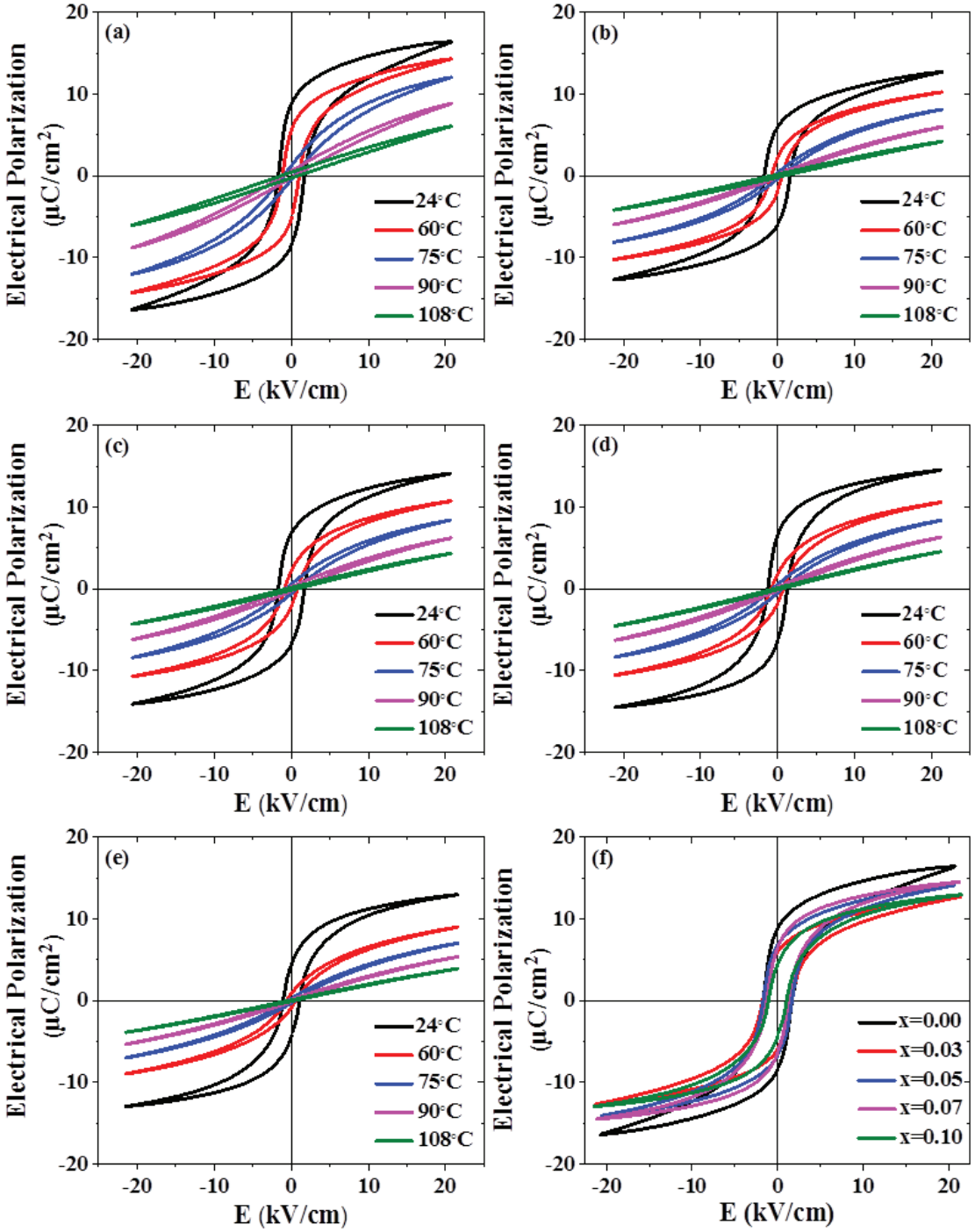

Figure 3.10. The P-E loops of $BSTZ_x$ ceramics for (a) x=0, (b) x=0.03, (c) x=0.05, (d) x=0.07, (e) x=0.10 and (f) comparison of all ceramics at 24°C and 1 Hz.

3.6. Calculation of the Electrocaloric Temperature Change

Temperature dependence of electrical polarization (P-T plots) extracted from the P-E hysteresis loops are plotted at different electric fields ranging from 0 to 20 kV/cm as shown in Figure 3.11 (a)-(e).

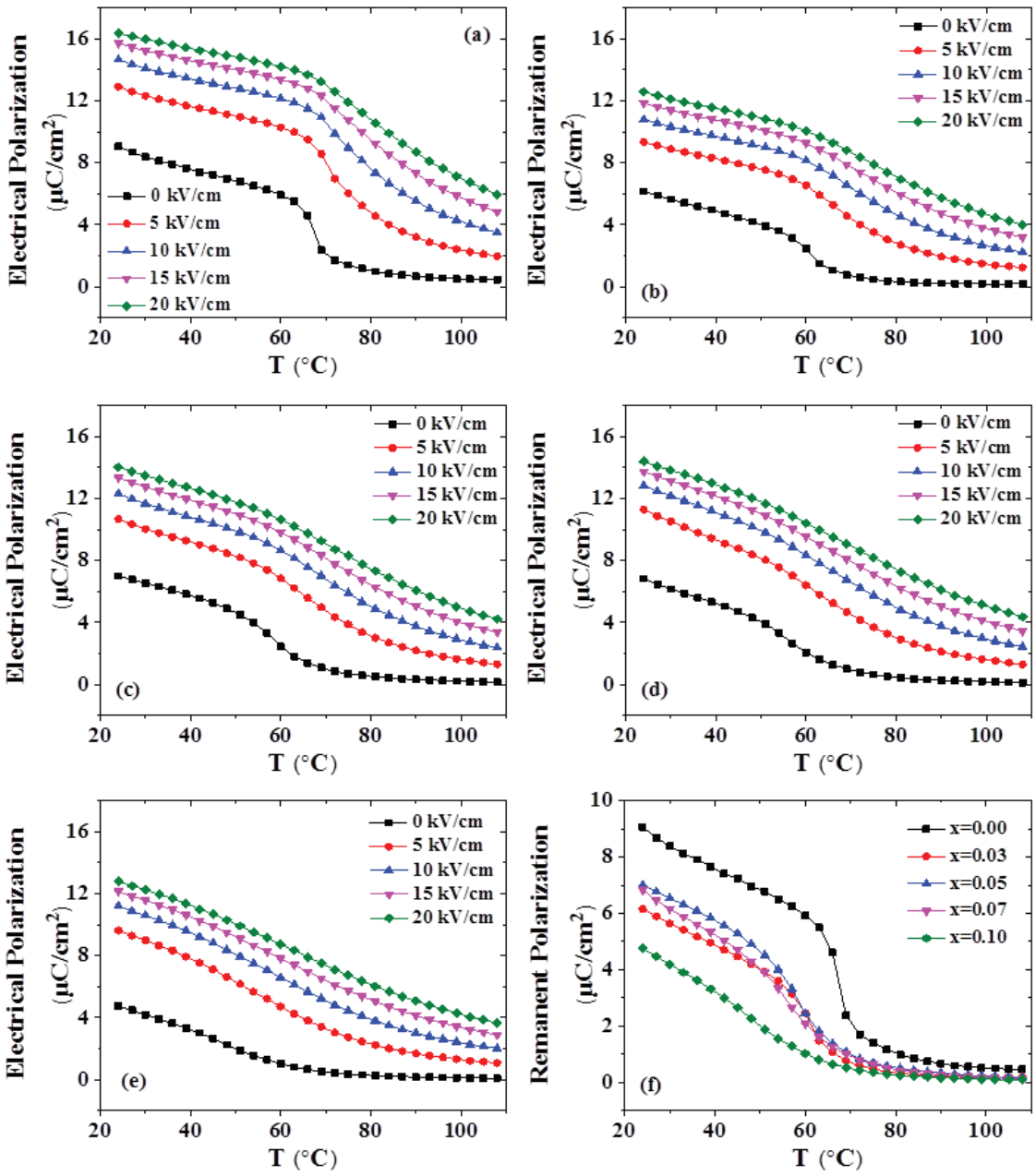

Figure 3.11. The P-T curves of $BSTZ_x$ with (a) x=0, (b) x=0.03, (c) x=0.05, (d) x=0.07, (e) x=0.10 at various electric fields and 1 Hz and (f) comparison of remanent polarization of all compositions.

For all compositions, the polarization increases with increasing electric field while the increase of the temperature causes a decrease in the polarization. It was also noticed that the change in the electric field affected the polarization behaviour near the Curie temperature. The sudden decrease in the polarization at 0 kV/cm near the T_c, was broadened by rising the electric field. The increase in electric field causes shifting of the

polarization to higher temperatures and therefore T_c increases for all samples under electric field.

Figure 3.11 (f) shows the remanent polarization values and how the polarization changes with respect to the composition close to the T_c. With the increase in the amount of Zr, T_c decreases and the sudden decrease in the polarization near the T_c was broadened. This is related to a transition from a first order to diffuse phase transition character as will be discussed below.[32]

The ΔT and the isothermal entropy change (ΔS) were numerically calculated by using the following Maxwell's relationships using Equations (3.3) and (3.4):[2] $(\frac{\partial P}{\partial T})$ term in these expressions was calculated numerically using Equation (3.5).[28]

$$\Delta T = -\frac{T}{\rho C_p}\int_{E_1}^{E_2}\left(\frac{\partial P}{\partial T}\right)_E dE \quad \textbf{(3.3)}$$

$$\Delta S = -\frac{1}{\rho}\int_{E_1}^{E_2}\left(\frac{\partial P}{\partial T}\right)_E dE \quad \textbf{(3.4)}$$

$$\left(\frac{\partial P}{\partial T}\right)_E = \left(\frac{1}{2}\right) * \left(\frac{P_n - P_{n-1}}{T_n - T_{n-1}} + \frac{P_{n+1} - P_n}{T_{n+1} - T_n}\right) \quad \textbf{(3.5)}$$

where ρ is density of ceramic, E_1 (0 kV/cm) and E_2 are initial and final electric field, respectively. The heat capacity C_p value was taken as 0.50 J g^{-1} K^{-1} for all $BSTZ_x$ compositions using $BaTiO_3$ based ferroelectric ceramic materials in the literature.[3,41,51]

Figure 3.12 (a)-(e) displays electrocaloric effect (ECE) or adiabatic temperature change (ΔT) as a function of temperature for $BSTZ_x$ ceramics at different electric fields ranging from 5 to 20 kV/cm. Calculated ΔT values are 0.62, 0.42, 0.43, 0.40 and 0.35 K for x=0.00, 0.03, 0.05, 0.07 and 0.10, respectively near the T_c at 20 kV/cm. For each ceramic, the increase in the electric field caused the increase of ΔT values and also peak broadening.

Figure 3.13 (a) exhibits the electrocaloric temperature change ΔT as a function of temperature for all $BSTZ_x$ ceramics at 20 kV/cm electric field and 1 Hz. The ΔT value of the undoped BST ceramic is higher than Zr substituted compositions. The increase in amount of Zr causes the peak broadening and decrease in the T_c. Also, the isothermal entropy change ΔS in Figure 3.13 (b) is consistent with the ΔT behaviour.

Calculated ΔS values are 0.88, 0.59, 0.61, 0.57 and 0.52 K for x=0.00, 0.03, 0.05, 0.07 and 0.10, respectively near the T_c at 20 kV/cm.

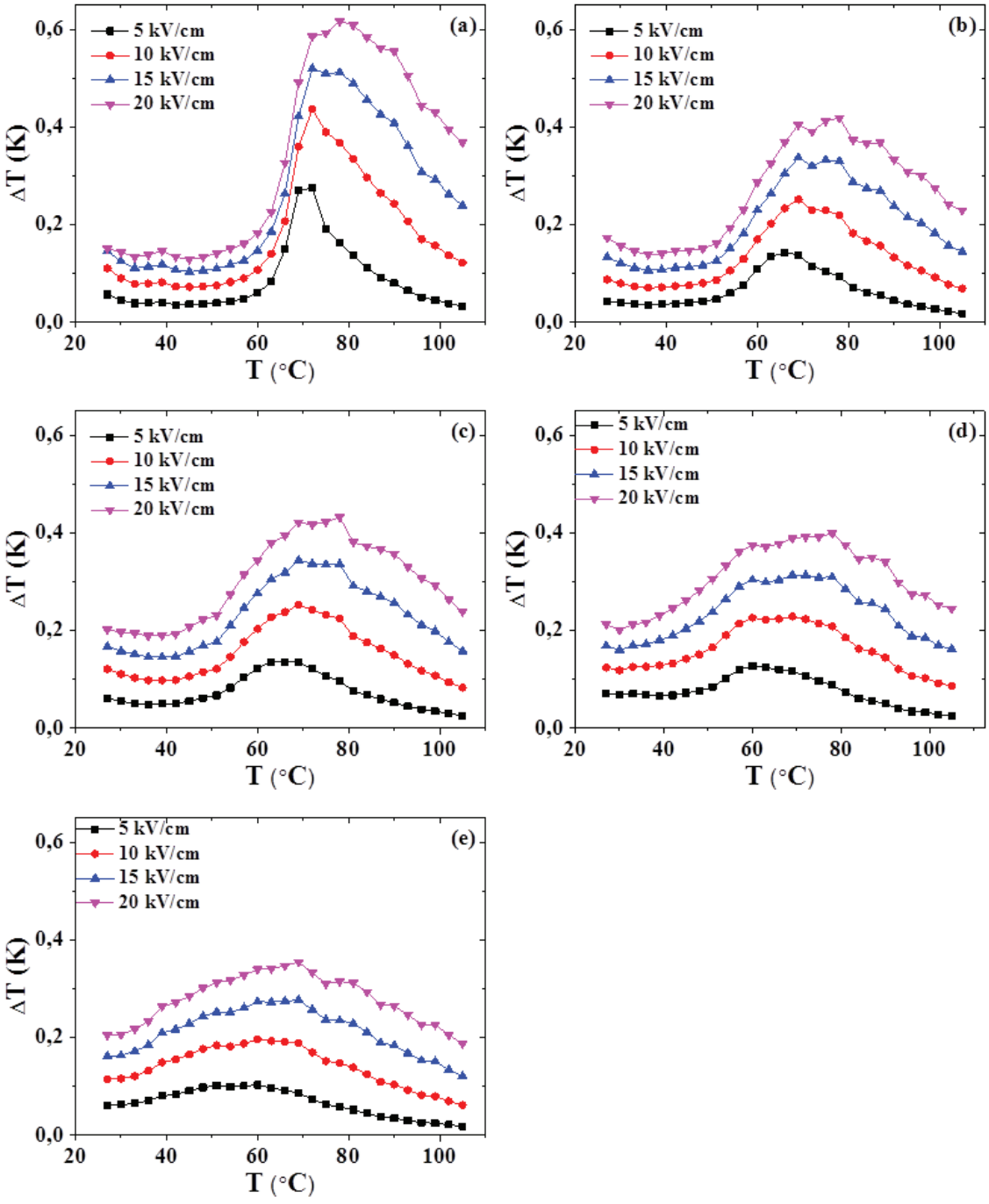

Figure 3.12. Numerically calculated ΔT-T curves of $BSTZ_x$ with (a) x=0, (b) x=0.03, (c) x=0.05, (d) x=0.07, (e) x=0.10 at various electric fields and 1 Hz.

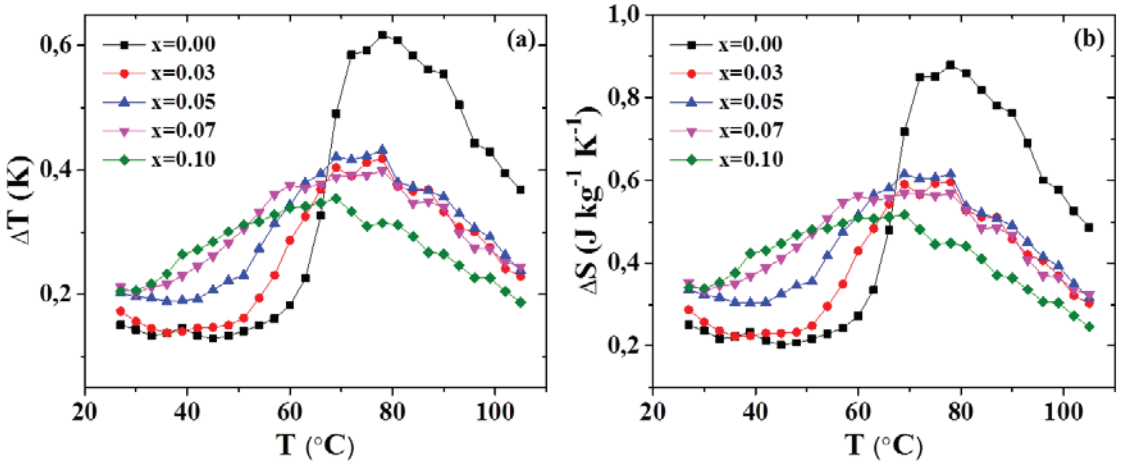

Figure 3.13. Temperature dependence of (a) ΔT and (b) ΔS at 20 kV/cm and 1 Hz.

The calculation of the EC temperature change (ΔT) was repeated by using P-T curves that are fitted using a fourth order polynomial. The reason for using two different methods in ΔT calculations is to differentiate between artificial anomalies caused by imperfect fitting and real sample behaviour. Figure 3.14 (a)-(e) displays the fitted P-T curves at 20 kV/cm and 1 Hz. Black symbols are the experimental points and red line is fitted curve.

It can be easily seen that the increase in amount of Zr facilitates the P-T curves to be more easily fitted. This is related to a transition from a first order to diffuse phase character. Due to the increase in the Zr substitution, the sudden drop in polarization around Tc was broadened and so P-T curves was fitted easily.

For all ceramic compositions, the ΔT-T curves as described in Figure 3.15 (a)-(e) were obtained at different electric fields ranging from 5 to 20 kV/cm and at 1 Hz by using the fitted P-T curves. When the comparison plot of the fitted ΔT-T for all compositions in Figure 3.15 (f) is examined, the values and the behaviour are consistent with the ΔT values that were calculated numerically in Figure 3.13 (a). Therefore, ΔT values calculated with both methods are compatible, showing the goodness of the fits.

Table 3.4 summarizes the comparison of the ECE properties of the $BSTZ_x$ ceramics studied in this work with those in the literature. For this work, it could be seen that the ΔT of the undoped BST ceramic is higher than the other compositions doped with Zr. The Zr substitution of the B-site on the perovskite causes disorder at B-site and a decrease in the tetragonality.[46] This behaviour was demonstrated by XRD measurements in Figure 3.2. Therefore, the ECE properties are expected to be high for

the undoped BST ceramic as it shows the first order phase transition according to discontinuous/sharp drop of remanent polarization at T_c.

When the maximum ΔT values of the Zr-doped compositions are compared, it can be seen that peak ΔT value of x=0.05 composition is greater than the other Zr doped ceramics.

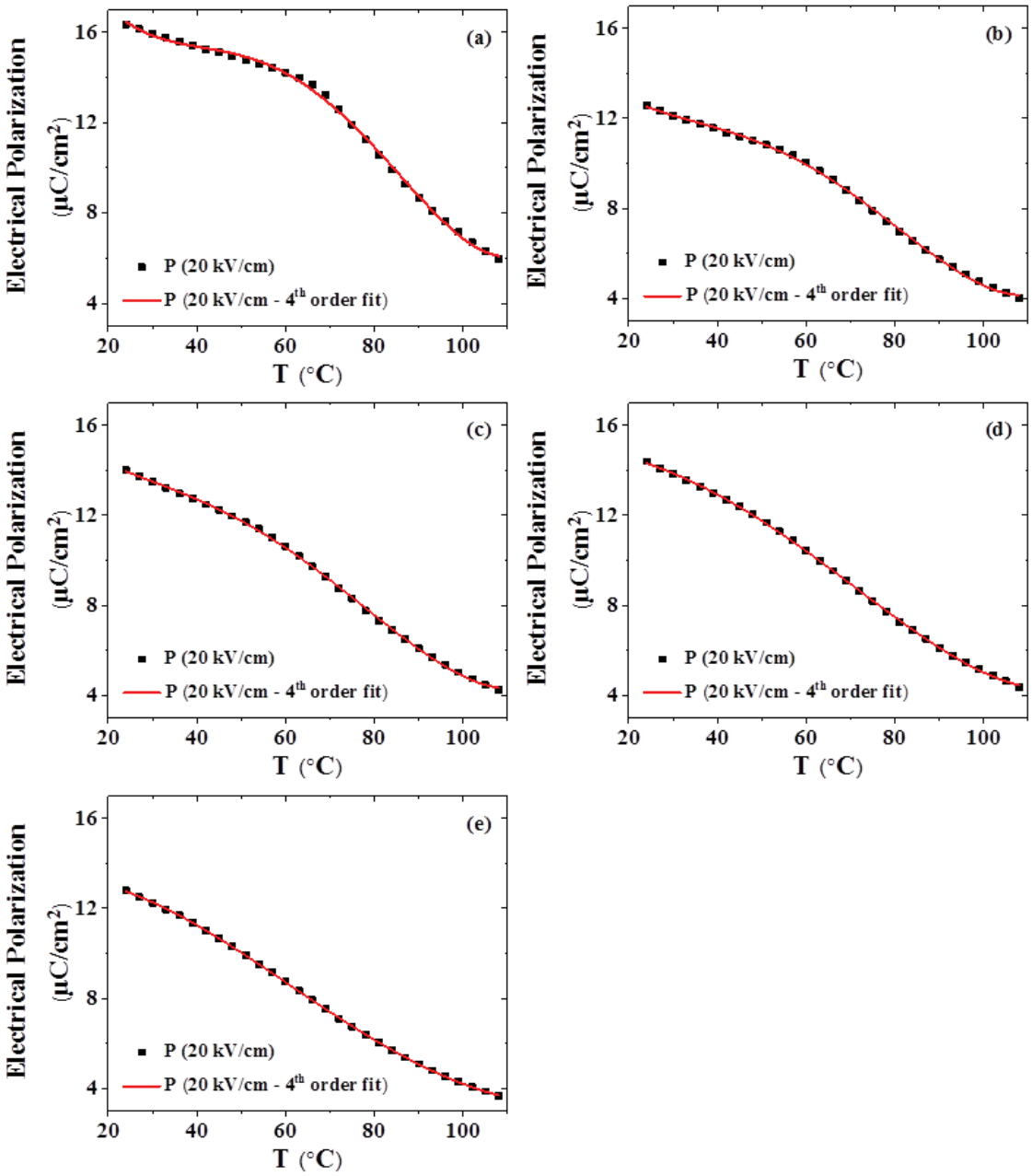

Figure 3.14. Fitted P-T curves of $BSTZ_x$ with (a) x=0, (b) x=0.03, (c) x=0.05, (d) x=0.07, (e) x=0.10 at 20 kV/cm electric field and 1 Hz.

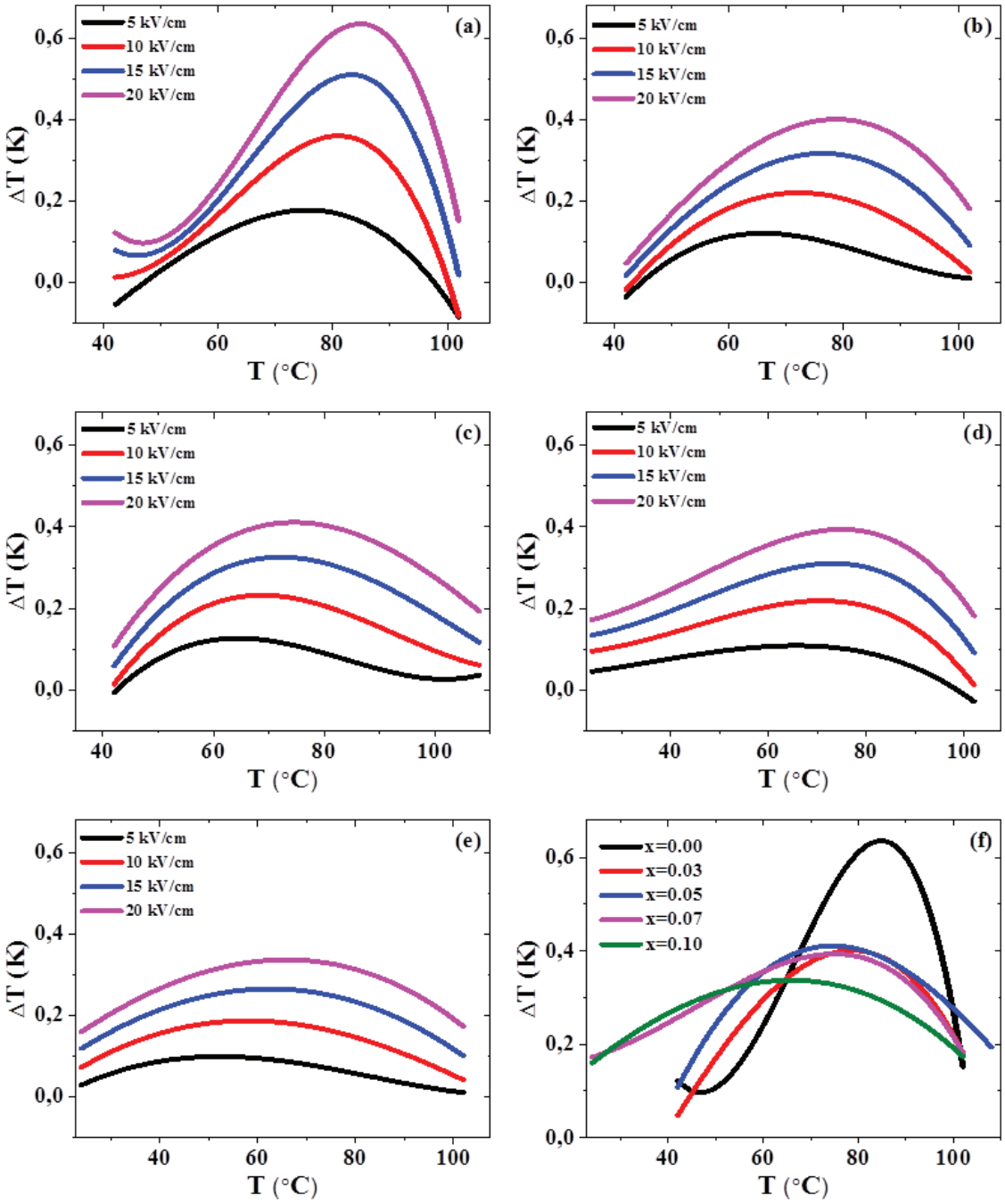

Figure 3.15. Fitted ΔT-T curves of $BSTZ_x$ with (a) x=0, (b) x=0.03, (c) x=0.05, (d) x=0.07, (e) x=0.10 at various electric fields and 1 Hz and (f) comparison of the fitted ΔT-T for all ceramics at 20 kV/cm.

According to the phase diagram shown in Figure 3.9, phase transition temperatures (T_{O-R}, T_{T-O}, T_{C-T}) become close to each other, resulting in multiphase coexistence, therefore the entropy change (ΔS) increases at x=0.05. Also, when the SEM micrographs are observed in the Figure 3.4, the grain size of x=0.05 ceramic is larger than x=0.03. It is known that larger grain sizes enhance the properties of ECE,

because decrease in grain boundary density strengthens the ferroelectricity. It should be noted that ECE properties of $BaTiO_3$ single crystal are larger than polycrystalline ceramics.[7]

Table 3.4. Comparison of the ECE properties of the $BSTZ_x$ ceramics studied in this work with those in the literature.

Material	T_c (K)	ΔT (K)	ΔE (kV/cm)	$\Delta T/\Delta E$ (K.mm/kV)	Method	Ref.
$BaTiO_3$, single crystal	402	0.9	12	0.75	Direct	[6]
$BaTiO_3$, ceramic	398	1.1	20	0.56	Indirect	[4]
$Ba_{0.65}Sr_{0.35}TiO_3$, ceramic	296	0.42	20	0.21	Indirect	[7]
$Ba_{0.94}Ca_{0.06}Ti_{0.875}Sn_{0.125}O_3$, ceramic	298	0.24	6	0.4	Indirect	[52]
$BaTi_{0.89}Hf_{0.11}O_3$, ceramic	343	0.35	10	0.35	Indirect	[32]
$Ba_{0.8}Ca_{0.2}Ti_{0.96}Zr_{0.04}O_3$, ceramic	386	0.27	7.95	0.34	Indirect	[46]
$BaSn_{0.1}Ti_{0.9}O_3$, ceramic	337	0.48	15	0.32	Indirect	[26]
$Ba_{0.8}Sr_{0.2}TiO_3$, ceramic	345	0.44	10	0.44	Indirect	This work
$Ba_{0.8}Sr_{0.2}TiO_3$, ceramic	351	0.62	20	0.31	Indirect	This work
$Ba_{0.8}Sr_{0.2}Ti_{0.97}Zr_{0.03}O_3$, ceramic	342	0.25	10	0.25	Indirect	This work
$Ba_{0.8}Sr_{0.2}Ti_{0.97}Zr_{0.03}O_3$, ceramic	351	0.42	20	0.21	Indirect	This work
$Ba_{0.8}Sr_{0.2}Ti_{0.95}Zr_{0.05}O_3$, ceramic	342	0.25	10	0.25	Indirect	This work
$Ba_{0.8}Sr_{0.2}Ti_{0.95}Zr_{0.05}O_3$, ceramic	351	0.43	20	0.215	Indirect	This work
$Ba_{0.8}Sr_{0.2}Ti_{0.93}Zr_{0.07}O_3$, ceramic	342	0.23	10	0.23	Indirect	This work
$Ba_{0.8}Sr_{0.2}Ti_{0.93}Zr_{0.07}O_3$, ceramic	351	0.40	20	0.20	Indirect	This work
$Ba_{0.8}Sr_{0.2}Ti_{0.90}Zr_{0.10}O_3$, ceramic	333	0.20	10	0.20	Indirect	This work
$Ba_{0.8}Sr_{0.2}Ti_{0.90}Zr_{0.10}O_3$, ceramic	342	0.35	20	0.175	Indirect	This work

Since x = 0.07 sample is the closest composition to the critical point of the phase diagram, different ferroelectric phases coexist at this composition. Its dielectric constant

is the highest among others because the material can be polarized along the polarization directions in each of these phases. Similar to our case, Li et al.[32] has reported that $BaHf_xTi_{1-x}O_3$ ceramics shows the largest dielectric maximum for a composition at located at the critical point. However, in that case, they also obtained largest ΔT for the same composition. On the other hand, in our study ΔT value of x=0.07 composition is smaller than x=0.0 and x=0.05 compositions. This might be related with the specific heat value that we use to calculate ΔT. We were not able to measure specific heat accurately and we assumed a constant value from the earlier studies for all compositions. Specific heat values for different compositions might differ slightly. Nevertheless, this slight difference might have changed the order of ΔT with composition.

According to the γ coefficients, it could be seen that x=0.10 ceramic shows diffuse phase transition, therefore $\left(\frac{\partial P}{\partial T}\right)$ is low. For this reason, although the grain sizes of x=0.07 and x=0.10 ceramics are larger than others, the ΔT values of these ceramics are smaller than other ceramics.

CHAPTER 4

CONCLUSIONS

The goal of this work was the determination of the electrocaloric temperature change (ΔT) values of lead-free $Ba_{0.8}Sr_{0.2}Ti_{1-x}Z_xO_3$ ceramics for $0 \leq x \leq 0.10$ by using the phase diagram from Szymczak et al.

When all the results were evaluated, it was evident that the electrocaloric behaviour changes at different regions of the phase diagram. Zr substitution caused a decrease in tetragonality and a phase transition character changes from first order to diffuse type. This causes a decrease in the ΔT values while expanding the operating temperature range of ECE. In the region where the first order phase transition is effective, the sharpness of the change in temperature-dependent polarization narrows the operating temperature range which may restrict the applicability of ECE.

When the obtained ΔT values are compared, the x=0.07 composition with large operating temperature range and relatively large ΔT value is considered to be the optimum composition. The ΔT value has been found as 0.40 K under 20 kV/cm electric field at 351 K for this composition. Based on these results, and in comparison with the other doped $BaTiO_3$ systems, $Ba_{0.8}Sr_{0.2}Ti_{1-x}Z_xO_3$ system can be considered as one of the best candidates for future electrocaloric cooling applications.

REFERENCES

(1) Valant, M. Electrocaloric Materials for Future Solid-State Refrigeration Technologies. *Prog. Mater. Sci.* **2012**, *57* (6), 980–1009.

(2) Mischenko, A. S.; Zhang, Q.; Scott, J. F.; Whatmore, R. W.; Mathur, N. D. Giant Electrocaloric Effect in PZT. *Science.* **2006**, *104* (1), 9–13.

(3) Kaddoussi, H.; Gagou, Y.; Lahmar, A.; Allouche, B.; Dellis, J. L.; Courty, M.; Khemakhem, H.; El Marssi, M. Ferroelectric Phase Changes and Electrocaloric Effects in $Ba(Zr_{0.1}Ti_{0.9})_{1-x}$ Sn_x O_3 Ceramics Solid Solution. *J. Mater. Sci.* **2016**, *51* (7), 3454–3462.

(4) Ren, X.-C.; Nie, W.-L.; Bai, Y.; Qiao, L.-J. Effect of Sintering Temperature and Oxygen Atmosphere on Electrocaloric Effect of $BaTiO_3$ Ceramics. *Eur. Phys. J. B.* **2015**, *88* (9), 232.

(5) Luo, Z.; Zhang, D.; Liu, Y.; Zhou, D.; Yao, Y.; Liu, C.; Dkhil, B.; Ren, X.; Lou, X. Enhanced Electrocaloric Effect in Lead-Free $BaTi_{1-x}Sn_xO_3$ Ceramics near Room Temperature. *Appl. Phys. Lett.* **2014**, *105* (10), 102904.

(6) Moya, X.; Stern-Taulats, E.; Crossley, S.; González-Alonso, D.; Kar-Narayan, S.; Planes, A.; Mañosa, L.; Mathur, N. D. Giant Electrocaloric Strength in Single-Crystal $BaTiO_3$. *Adv. Mater.* **2013**, *25* (9), 1360–1365.

(7) Bai, Y.; Han, X.; Ding, K.; Qiao, L. J. Combined Effects of Diffuse Phase Transition and Microstructure on the Electrocaloric Effect in $Ba_{1-x}Sr_xTiO_3$ Ceramics. *Appl. Phys. Lett.* **2013**, *103* (16).

(8) Qian, X. S.; Ye, H. J.; Zhang, Y. T.; Gu, H.; Li, X.; Randall, C. A.; Zhang, Q. M. Giant Electrocaloric Response over a Broad Temperature Range in Modified $BaTiO_3$ Ceramics. *Adv. Funct. Mater.* **2014**, *24* (9), 1300–1305.

(9) Correia, T.; Zhang, Q. *Electrocaloric Materials: New Generation of Coolers*; **2014**; pp 147-182.

(10) Kutnjak, Z.; Rožič, B.; Pirc, R. Electrocaloric Effect: Theory, Measurements and Applications, Published March 16, **2015**. https://onlinelibrary.wiley.com/doi/10.1002/047134608X.W8244 (accessed Jan 25, 2019).

(11) Takeuchi, I.; Sandeman, K. Solid-State Cooling with Caloric Materials. *Phys. Today.* **2015**, *68* (12), 48–54.

(12) The Greenhouse Effect. http://www.ces.fau.edu/nasa/module-2/how-greenhouse-effect-works.php (accessed Jan 21, 2019).

(13) Katz, B. G.; Griffin, D. W. Using Chemical and Microbiological Indicators to

Track the Impacts from the Land Application of Treated Municipal Wastewater and Other Sources on Groundwater Quality in a Karstic Springs Basin. *Environ. Geol.* **2008**, *55* (4), 801–821.

(14) Ma, R.; Zhang, Z.; Tong, K.; Huber, D.; Kornbluh, R.; Ju, Y. S.; Pei, Q. Highly Efficient Electrocaloric Cooling with Electrostatic Actuation. *Science*. **2017**, *357*, 1130–1134.

(15) Liu, Y.; Scott, J. F.; Dkhil, B. Some Strategies for Improving Caloric Responses with Ferroelectrics. *APL Mater.* **2016**, *4* (6), 0–9.

(16) Moya, X.; Kar-Narayan, S.; Mathur, N. D. Caloric Materials near Ferroic Phase Transitions. *Nat. Mater.* **2014**, *13* (5), 439–450.

(17) Jaffe, B.; Jaffe, H. *Piezoeletric Ceramics*; **1971**; p 94.

(18) Valant, M.; Dunne, L. J.; Axelsson, A. K.; Alford, N. M. N.; Manos, G.; Peräntie, J.; Hagberg, J.; Jantunen, H.; Dabkowski, A. Electrocaloric Effect in a Ferroelectric $Pb(Zn_{1/3}Nb_{2/3})O_3$-$PbTiO_3$ Single Crystal. *Phys. Rev. B - Condens. Matter Mater. Phys.* **2010**, *81* (21), 18–22.

(19) Zhang, R.; Peng, S.; Xiao, D.; Wang, Y.; Yang, B.; Zhu, J.; Yu, P.; Zhang, W. Preparation and Characterization of (1-x)$Pb(Mg_{1/3}Nb_{2/3})O_3$-x$PbTiO_3$ Electrocaloric Ceramics. *Cryst. Res. Technol.* **1998**, *33* (5), 827–832.

(20) Liu, S.; Li, Y. Research on the Electrocaloric Effect of PMN/PT Solid Solution for Ferroelectrics MEMS Microcooler. *Mater. Sci. Eng. B Solid-State Mater. Adv. Technol.* **2004**, *113* (1), 46–49.

(21) Sebald, G.; Seveyrat, L.; Guyomar, D.; Lebrun, L.; Guiffard, B.; Pruvost, S. Electrocaloric and Pyroelectric Properties of 0.75$Pb(Mg_{1/3}Nb_{2/3})O_3$-0.25$PbTiO_3$ Single Crystals. *J. Appl. Phys.* **2006**, *100* (12), 0–6.

(22) Saranya, D.; Chaudhuri, A. R.; Parui, J.; Krupanidhi, S. B. Electrocaloric Effect of PMN-PT Thin Films near Morphotropic Phase Boundary. *Bull. Mater. Sci.* **2009**, *32* (3), 259–262.

(23) Neese, B.; Chu, B.; Lu, S. G.; Wang, Y.; Furman, E.; Zhang, Q. M. Large Electrocaloric Effect in Ferroelectric Polymers near Room Temperature. *Science.* **2008**, *321* (5890), 821–823.

(24) Upadhyay, S. K.; Fatima, I.; Reddy, V. R. Study of Electro-Caloric Effect in Ca and Sn Co-Doped $BaTiO_3$ Ceramics. *Mater. Res. Express* **2017**, *4* (4), 46303.

(25) Wang, X.; Wu, J.; Dkhil, B.; Zhao, C.; Li, T.; Li, W.; Lou, X. Large Electrocaloric Strength and Broad Electrocaloric Temperature Span in Lead-Free $Ba_{0.85}Ca_{0.15}Ti_{1-x}Hf_xO_3$ Ceramics. *RSC Adv.* **2017**, *7* (10), 5813–5820.

(26) Qi, S.; Zhang, G.; Duan, L.; Zeng, T.; Cao, J. Electrocaloric Effect in Pb-Free Sr-Doped $BaTi_{0.9}Sn_{0.1}O_3$ Ceramics. *Mater. Res. Bull.* **2017**, *91*, 31–35.

(27) Patel, S.; Chauhan, A.; Vaish, R. Electrocaloric Behavior and Temperature-Dependent Scaling of Dynamic Hysteresis of $Ba_{0.85}Ca_{0.15}Ti_{0.9}Zr_{0.1}O_3$ Ceramics. *Int. J. Appl. Ceram. Technol.* **2015**, *12* (4), 899–907.

(28) Goupil, F. Le. Electrocaloric Effect in Ferroelectric Relaxors : The Road to Solid-State Cooling. Imperial Collage London, **2013**.

(29) Setter, N. What Is a Ferroelectric – a Materials Designer Perspective. *Ferroelectrics.* **2016**, *500* (1), 164–182.

(30) Whatmore, R. Electronic and Photonic Materials: Ferroelectric Materials, 2nd ed. pp 597–623.

(31) Damjanovic, D. Ferroelectric , Dielectric and Piezoelectric Properties of Ferroelectric Thin Films and Ceramics. *Reports on Progress in Physics.* **1998**, *61*, 1267-1324.

(32) Li, J.; Zhang, D.; Qin, S.; Li, T.; Wu, M.; Wang, D.; Bai, Y.; Lou, X. Large Room-Temperature Electrocaloric Effect in Lead-Free $BaHf_xTi_{1-x}O_3$ Ceramics under Low Electric Field. *Acta Mater.* **2016**, *115*, 58–67.

(33) Luisman, L.; Feteira, A.; Reichmann, K. Weak-Relaxor Behaviour in Bi/Yb-Doped $KNbO_3$ Ceramics. *Appl. Phys. Lett.* **2011**, *99* (19), 2012–2015.

(34) Wang, C.-M.; Lau, K.; Wang, Q. Dynamic Hysteresis and Scaling Behaviours of Lead-Free $0.94Bi_{0.5}Na_{0.5}TiO_3$ –$0.06BaTiO_3$ Bulk Ceramics. *RSC Adv.* **2016**, *6* (36), 30148–30153.

(35) Delgado, M. Phase Transitions in Relaxor Ferroelectrics. **2005**, 1–11. http://guava.physics.uiuc.edu/~nigel/courses/563/Essays_2005/PDF/delgado.pdf (accessed Jan 25, 2019).

(36) Li, T.; Liu, X.; Shi, S.; Yin, Y.; Li, H.; Wang, Q.; Zhang, Y.; Bian, J.; Rajput, S. S.; Long, C. Large Electrocaloric Efficiency over a Broad Temperature Span in Lead-Free $BaTiO_3$-Based Ceramics near Room Temperature. *Appl. Phys. Lett.* **2017**, *111* (20), 0–5.

(37) Thacher, P. D. Electrocaloric Effects in Some Ferroelectric and Antiferroelectric Pb(Zr, Ti)O_3 Compounds. *J. Appl. Phys.* **1968**, *39* (4), 1996–2002.

(38) Rožić, B.; Malić, B.; Uršič, H.; Holc, J.; Kosec, M.; Kutnjak, Z. Direct Measurements of the Electrocaloric Effect in Bulk $PbMg_{1/3}Nb_{2/3}O_3$ (PMN) Ceramics. *Ferroelectrics* **2011**, *421* (1), 103–107.

(39) Szymczak, L.; Adamczyk, M.; Pawelczyk, M. Dielectric and Pyroelectric Properties of Zr-Doped $(Ba_{0.8}Sr_{0.2})TiO_3$ Ceramics. *Archives of Metallurgy and Materials*. 2009, *54*, 107–108.

(40) Liu, X. Q.; Chen, T. T.; Wu, Y. J.; Chen, X. M. Enhanced Electrocaloric Effects

in Spark Plasma-Sintered $Ba_{0.65}Sr_{0.35}TiO_3$-Based Ceramics at Room Temperature. *J. Am. Ceram. Soc.* **2013**, *96* (4), 1021–1023.

(41) Liu, X. Q.; Chen, T. T.; Fu, M. Sen; Wu, Y. J.; Chen, X. M. Electrocaloric Effects in Spark Plasma Sintered $Ba_{0.7}Sr_{0.3}TiO_3$-Based Ceramics: Effects of Domain Sizes and Phase Constitution. *Ceram. Int.* **2014**, *40* (7), 11269–11276.

(42) Smart, L. E.; Moore, E.A. *Solid State Chemistry: An Introduction*, 3rd ed.; 2005; p 1.

(43) Degen, T.; Sadki, M.; Bron, E.; König, U.; Nénert, G. The HighScore Suite. *Powder Diffr.* **2014**, *760* (May), 13–18.

(44) Chinn , R. E. *Ceramography: Preparation and Analysis of Ceramic Microstructures*. **2002**; pp 45-54.

(45) Callister, W.; Rethwisch, D. Materials Science: An Introduction, 9th ed. **2013**; pp 759-767.

(46) Asbani, B.; Dellis, J.-L.; Lahmar, A.; Courty, M.; Amjoud, M.; Gagou, Y.; Djellab, K.; Mezzane, D.; Kutnjak, Z.; El Marssi, M. Lead-Free $Ba_{0.8}Ca_{0.2}(Zr_x Ti_{1-x})O_3$ Ceramics with Large Electrocaloric Effect. *Appl. Phys. Lett.* **2015**, *106* (4), 42902.

(47) Periodic Table of Elements and X-Ray Energies. https://www.bruker.com/fileadmin/user_upload/8-PDF-Docs/X-rayDiffraction_ElementalAnalysis/HH-XRF/Misc/Periodic_Table_and_X-ray (accessed Jan 25, 2019).

(48) Mohan, C. R. K.; Bajpai, P. K. Effect of Sintering Optimization on the Electrical Properties of Bulk $Ba_xSr_{1-x}TiO_3$ Ceramics. *Phys. B Condens. Matter* **2008**, *403* (13–16), 2173–2188.

(49) Kytae, T.; Sutjarittangtham, K.; Thurakitseree, T.; Leenakul, W. Phase Transition and Electrical Properties of $Ba_{0.8}Sr_{0.2}TiO_3$ Comparison of Different Preparation Techniques. *Appl. Mech. Mater.* **2017**, *866*, 287–290.

(50) Zhang, X.; Wu, L.; Gao, S.; Liu, J. Q.; Xu, B.; Xia, Y. D.; Yin, J.; Liu, Z. G. Large Electrocaloric Effect in $Ba(Ti_{1-x}Sn_x)O_3$ Ceramics over a Broad Temperature Region. *AIP Adv.* **2015**, *5* (4), 1–8.

(51) Morimoto, K.; Sawai, S.; Hisano, K.; Yamamoto, T. Simultaneous Measurement of Specific Heat, Thermal Conductivity, and Thermal Diffusivity of Modified Barium Titanate Ceramics. *Thermochim. Acta* **2006**, *442* (1–2), 14–17.

(52) Wang, X.; Tian, F.; Zhao, C.; Wu, J.; Liu, Y.; Dkhil, B.; Zhang, M.; Gao, Z.; Lou, X. Giant Electrocaloric Effect in Lead-Free $Ba_{0.94}Ca_{0.06}Ti_{1-x}Sn_xO_3$ Ceramics with Tunable Curie Temperature. *Appl. Phys. Lett.* **2015**, *107* (25), 252905.